

The observed spatio-temporal patterns of Land surface temperature over the Contiguous United States

Laura Torres-Rojas¹, Tyler Waterman², Jiaxuan Cai¹, Enrico Zorzetto³, Haruko Murakami Wainwright⁴, and Nathaniel W. Chaney¹

¹Duke University

²Duke University Civil and Environmental Engineering

³Princeton University

⁴Lawrence Berkeley National Laboratory

October 30, 2023

1 **The observed spatio-temporal patterns of Land surface temperature over the**
2 **Contiguous United States**

3 **L. Torres-Rojas¹, T. Waterman¹, J. Cai¹, E. Zorzetto², H.M. Wainwright^{3,4}, and N. W.**
4 **Chaney¹**

5 ¹ Department of Civil and Environmental Engineering, Duke University, Durham, NC, United
6 States of America.

7 ² Program in Atmospheric and Oceanic Sciences, Princeton University, Princeton, NJ, United
8 States of America.

9 ³ Earth and Environmental Sciences Area, Lawrence Berkeley National Laboratory, Berkeley,
10 CA, United States of America.

11 ⁴ Massachusetts Institute of Technology, Cambridge, MA, United States of America.

12

13 Corresponding author: Laura Torres-Rojas (laura.torres@duke.edu)

14 **Key Points:**

- 15 • The Empirical Spatio-Temporal Covariance Function is a flexible tool to describe the
16 spatiotemporal dependence structure of observed fields.
- 17 • A parametric covariance model can concisely describe the spatio-temporal patterns
18 captured from empirical data.
- 19 • Multidimensional clustering can be used to identify areas with similar spatiotemporal
20 dependence structures over continental scales.
- 21

22 **Abstract**

23 Surface fluxes and their related processes and states tend to recur and remain consistent across
24 various spatial and temporal scales forming patterns. For multiple applications, identifying
25 spatio-temporal patterns is desirable, as they provide information about the dynamics of the
26 processes involved. This is especially true for land surface temperature, a key variable that plays
27 a primary role in the energy and water exchange between land and atmosphere. This study
28 introduces the Empirical Spatio-Temporal Covariance Function (ESTCF) as a tool to identify
29 and characterize spatio-temporal patterns in remotely sensed land surface temperature fields. The
30 method is demonstrated over the Contiguous United States by splitting the entire area into
31 $1.0^{\circ} \times 1.0^{\circ}$ domains. The summer day-time surface temperature ESTCFs are derived for each
32 domain, and a parametric covariance model is fitted. Clustering analysis is then applied to detect
33 areas with similar spatio-temporal land surface temperature dynamics. The results are assessed to
34 determine if particular spatio-temporal features are present in domains where landscape
35 characteristics make interactions with the atmosphere likely. The proposed tool accurately
36 characterizes the spatio-temporal interdependence of the fields, summarizing features such as
37 spatio-temporal variance, spatial coherence structure, temporal persistence, and space-time
38 interactions. The increased temporal persistence and space-time interaction drive the grouping in
39 mountainous and coastal domains. The tools introduced here provide a pathway to formally
40 identify and summarize the spatio-temporal patterns observed in remotely sensed fields and
41 relate those to more complex processes within the Soil-Vegetation-Atmosphere System.

42

43 **Plain Language Summary**

44 Specific processes on Earth's surface, like heat and water fluxes and air movement, often exhibit
45 coherent patterns across space and time. Figuring out where these patterns occur can be helpful
46 as they can help explain how the underlying physical processes work. This research introduces a
47 new tool to find and describe these patterns and applies it to temperature data derived from
48 satellites. The United States is divided into smaller areas, and the developed tool is used to
49 analyze the land temperature data within those areas; then, regions with similar temperature
50 patterns are identified. These results help to determine if certain landscape features, like
51 coastlines, mountains, and cities, influence how temperature patterns behave. Ultimately, the
52 method can accurately describe how the temperature patterns vary over time, space, and both. As
53 expected, the results show that places with similar temperature patterns are often near coasts and
54 high mountains due to how temperature changes over time and interacts with its surroundings.
55 The tools presented here are a step toward better understanding how air, water, and heat move
56 near the Earth's surface, how they distribute in space, and how they change over time.

57 **1 Introduction**

58 Processes at the land-atmosphere interface are mainly driven by water and energy fluxes
59 at the land surface, which are mediated by vegetation (Koch et al., 2017; Simon et al., 2021),
60 land use, and topography. These surface fluxes have proved to control the overlying atmospheric
61 distributions of water vapor, temperature, precipitation, and cloud properties, modulating the
62 hydrological cycle and the surface energy budget (Dickinson, 1995; Dirmeyer et al., 2013; Y.
63 Wang et al., 2023; Wu et al., 2015). More specifically, the multi-scale spatial heterogeneity of
64 the physical environment (e.g., vegetation, soils, elevation, and land use) has been acknowledged

65 to influence the spatial and temporal distribution of the fluxes in a nonlinear manner (Dickinson,
66 1995; R. A. Fisher & Koven, 2020; Koch et al., 2017; Nicholson, 1988; Simon et al., 2021; Tesfa
67 et al., 2014; Torres-Rojas et al., 2022; Vergopolan et al., 2022). Besides, it is widely recognized
68 that certain fluxes and associated processes and variables tend to recur and appear consistently
69 across different scales in space, time, or both. These recurrent attributes are commonly referred
70 to as patterns, and they can be a consequence of the self-organization of the systems and the
71 organization in the systems' controlling factors (i.e., influence of the physical environment)
72 (Koch et al., 2017; Vereecken et al., 2016).

73 The dynamic processes producing patterns expand over a wide range of spatial and
74 temporal scales and encompass all compartments of the soil-vegetation-atmosphere system
75 (SVAS). Some processes are quasi-static in nature (e.g., bedrock generation, rising and sinking
76 motions of the Earth's mantle, and soil generation (Jenny, 1941)). On the global and synoptic
77 scales, quasi-static surface patterns such as land-sea distribution and orography are known to
78 control the spatial distribution of atmospheric variables such as precipitation, pressure, and
79 temperature (Vereecken et al., 2016). From the meso- to the micro-scale, topography also
80 induces cloud and precipitation patterns and orography-following flow patterns (e.g., Lee-wave
81 clouds and valley-slope wind systems) (Brunsell & Gillies, 2003; Paleri et al., 2022).
82 Furthermore, heterogeneity in vegetation and soil type distributions may cause patterns in the
83 surface fluxes, leading to lake breeze circulation systems that can impact cloud cover and
84 precipitation (Mahfouf et al., 1987; Nair et al., 2011). Finally, short-term atmospheric systems
85 can directly influence the soil and vegetation states by determining the soil moisture and
86 temperature distributions through precipitation and evapotranspiration patterns. Soil moisture
87 patterns are constrained by hydrological processes such as infiltration and runoff, dependent on
88 the quasi-static soil properties. Soil temperature is also directly intertwined with soil moisture
89 patterns and quasi-static soil thermal properties. Interestingly, soil moisture and temperature
90 patterns also play a crucial role in defining atmospheric stability and available moisture for
91 precipitation, making them critical in the two-way interactions between the atmosphere and the
92 land surface (Ferguson et al., 2012; Ferguson & Wood, 2011; Levine et al., 2016; Phillips et al.,
93 2017; Taylor et al., 2013; Tuttle & Salvucci, 2016). In general, patterns can be detected in a
94 variety of spatio-temporal fields, including hydraulic properties in soils (Chaney et al., 2016;
95 Gueting et al., 2015; Qu et al., 2014), surface soil moisture and soil temperature (Martini et al.,
96 2015; Poltoradnev et al., 2016; Seyfried et al., 2016; Vergopolan et al., 2021), latent and sensible
97 heat (Jung et al., 2011; Simon et al., 2021), convection-induced atmospheric boundary layer
98 (ABL) circulations (Taylor et al., 2007, 2011), and vegetation properties and states (Van der
99 Putten et al., 2013).

100 Several approaches have been developed to identify, summarize, and extract relevant
101 patterns from spatio-temporal geophysical datasets. The reader is referred to (Cressie & Wikle,
102 2015; Vereecken et al., 2016) for a detailed exploration of the approaches, their advantages, and
103 their information content. Some techniques are based on decomposing the spatial and temporal
104 signals according to their statistics or scales. Examples of decomposition approaches include the
105 Empirical Orthogonal Function (EOF) method, Principal Component Analysis (PCA),
106 Orthogonal Probability Density Function Decomposition (OPDFD), Wavelet Transform (WT),
107 and Empirical Mode Decomposition (EMD). These methods can be applied in both space and
108 time, and they have proved to be helpful in the simplification of complex datasets, the
109 decomposition and identification of relevant temporal signals, and the determination of critical
110 scales of processes within the SVAS (Biswas, 2014; Z. Fang et al., 2015; Graf et al., 2012; Katul

111 et al., 2001; Katul & Parlange, 1995; Kim & Barros, 2002; Koch et al., 2015; Korres et al., 2010;
112 Rudi et al., 2010; Stoy et al., 2005; Vargas et al., 2010; D. Wagner et al., 1990). However, in
113 general, they are only meant to analyze time and frequency dimensions.

114 For climate, environmental, and hydrological applications, the simultaneous
115 identification of spatially coherent persistent structures (i.e., spatio-temporal patterns) of the
116 relevant state variables is desirable, as they provide information about the dynamics of the
117 processes affecting them. In other words, the signatures of spatio-temporal processes in these
118 variables are not concrete, independent objects or events but patterns appearing and evolving
119 simultaneously over space and time (Faghmous & Kumar, 2014). For instance, let us consider
120 the distribution of inundation in a flooding-prone area. Multiple processes determine the
121 inundation dynamics within a watershed, including the spatio-temporal distribution of
122 precipitation, watershed-distributed physical characteristics (i.e., soil properties, antecedent soil
123 moisture content), and human modifications. The spatio-temporal evolution of the flooding as it
124 moves downstream due to re-infiltration, evaporation, preferential flow, and other processes
125 would be missed by looking only at the spatial or temporal dimensions independently (Cressie &
126 Wikle, 2015). Another case where the simultaneous space-time evolution of variables is pivotal
127 for process understanding is the initiation of heterogeneity-driven circulations at multiple scales.
128 Under favorable ABL and synoptic background conditions, larger spatial scales of surface
129 heterogeneity can generate temporally persistent structures of surface heating and moisture,
130 initiating circulations that for large enough scales, can produce areas of shallow or even deep
131 convection (F. Chen & Avissar, 1994; Cheng & Cotton, 2004; Courault et al., 2007; Gentine et
132 al., 2019; Pielke, 2001; Taylor et al., 2007; Weaver, 2004; Wu et al., 2015). The two previous
133 examples highlight the need for approaches that succinctly and effectively identify and
134 summarize the spatio-temporal patterns observed in climatic, environmental, and hydrological
135 datasets.

136 The geostatistics field has been concerned with addressing variables varying in space and
137 time for decades, primarily due to the improvement in predictions obtained by including
138 correlations in two dimensions instead of a single one (Cressie & Huang, 1999; Lee et al., 2010;
139 Rodríguez-Iturbe & Mejía, 1974; Rouhani & Myers, 1990; Varouchakis, 2018). Even though
140 geostatistics methods can make significant assumptions about the characteristics of the spatio-
141 temporal fields and associated patterns (i.e., stationarity, spatio-temporal dependence, isotropy,
142 and homoscedasticity, among others), they are still widely used as compact and straightforward
143 evaluation tools of the structure of the observation fields. Moving window sampling techniques
144 have been implemented to deal with the stationarity assumption (i.e., while environmental
145 phenomena exhibit heterogeneity in both their mean and covariance structure, it is often possible
146 to regard the process as approximately homogeneous within subregions) (Guttorp & Sampson,
147 1994; Haas, 1990a, 1990b; Risser & Turek, 2020). Among the tools developed for geostatistical
148 analysis, the empirical spatio-temporal covariance function (ESTCF) stands out for its simplicity.
149 Under the assumptions of second-order stationarity (i.e., the covariance between two points is the
150 same for a given distance and direction, regardless of which two points are chosen) in space and
151 time and isotropy in space, the ESTCF can be estimated directly from the observed data,
152 providing a measure of the strength and structure of dependence between different locations and
153 time points (W. Chen et al., 2021; Cressie & Huang, 1999; Faghmous & Kumar, 2014; Gneiting,
154 2002; Stein, 2005). The ESTCF is also able to capture various forms of dependence, such as
155 spatial correlation, temporal correlation, and spatio-temporal interactions (Cressie & Huang,
156 1999; Gneiting, 2002; Guttorp & Sampson, 1994; Ma, 2003; Stein, 2005). Finally, the method

157 can handle irregularly sampled data or missing values more effectively than other approaches
158 (e.g., spectral analysis), making it more suitable for real-world applications where data may be
159 sparse or irregularly collected (Demel & Du, 2015; Montero et al., 2015; Stein, 1999). Once the
160 ESTCF is computed, a parametric class of covariance model can be selected, and the parameters
161 estimated by fitting the model to the empirical function. This procedure allows learning about the
162 spatio-temporal properties and interactions of the original field from the estimated parameters
163 (W. Chen et al., 2021; Gneiting, 2002).

164 Traditional spatio-temporal geostatistical methods use a set of spatially-distributed in-situ
165 measurements to model the variation of the field of values as a function of the distance between
166 locations, reflecting Tobler's first law of geography: "Everything is related to everything else,
167 but near things are more related than distant things." (Tobler, 1970; Vereecken et al., 2016).
168 However, for regional and continental scales, widespread spatially distributed in situ
169 observations of surface fluxes and states do not exist (Stisen et al., 2011, 2021; Vereecken et al.,
170 2008; Zink et al., 2018). Hence, satellite remote sensing remains the only direct source of
171 spatially distributed Earth surface observations. Although the quantitative precision of this data
172 is still hard to determine, its main asset is its spatial and temporal information content over
173 extensive domains (Crow et al., 2009; H. T. Li et al., 2009; Stisen et al., 2011). Currently,
174 sensors onboard satellites provide spatially distributed estimates of several surface states,
175 including land surface temperature (LST) (L. Fang et al., 2014; Shi & Bates, 2011; Wan, 1996,
176 2014; Yu et al., 2012), soil moisture content (Chan et al., 2018; Entekhabi et al., 2010; Kerr et
177 al., 2012; Parinussa et al., 2015; W. Wagner et al., 2013), evapotranspiration (Boschetti et al.,
178 2019; J. B. Fisher et al., 2020; Martens et al., 2017; Running et al., 2019; Su, 2002), snow cover
179 fraction (Painter et al., 2009; Tsai et al., 2019), and changes in water storage (Tapley et al.,
180 2004). Therefore, the joint use of the ever-growing available remote sensing spatio-temporal data
181 and spatio-temporal geostatistics methods provides a promising path forward in the multi-scale
182 characterization of processes' heterogeneity and dynamics in multiple SVAS compartments.

183 A promising and relatively unexplored source of remote sensing data for the analysis of
184 spatio-temporal patterns of surface states on sub-diurnal scales is LST (Duffy et al., 2022; Koch
185 et al., 2016; Zink et al., 2018). As a critical state variable of the land surface, LST encodes
186 information on local energy and water fluxes, including energy partitioning into sensible and
187 latent heat fluxes (Duffy et al., 2022; Holzman et al., 2014; K. Li et al., 2021; Sims et al., 2008;
188 K. Wang & Dickinson, 2012). This information is vital as energy partitioning can affect the state
189 of the atmosphere by supplying water vapor, inducing convection and lateral convergence, and
190 growing the planetary boundary layer (Levine et al., 2016; Pielke, 2001; Tuttle & Salvucci,
191 2016). Recently, enhanced spatio-temporal resolution global LST products have been released,
192 including the ECOSystem Spaceborne Thermal Radiometer on the International Space Station
193 (ECOSTRESS) (Hook & Hulley, 2019), Landsat Provisional (Anderson et al., 2012), the
194 National Oceanic and Atmospheric Administration (NOAA) Geostationary Operational
195 Environmental Satellites (GOES) (L. Fang et al., 2014; Yu et al., 2012), and Sentinel-3
196 (Polehampton et al., 2022). However, increased spatial resolutions are often not accompanied by
197 enhanced temporal resolutions. Products derived from sensors onboard satellites with polar
198 orbits, such as NASA's Moderate Resolution Imaging Spectroradiometer (MODIS), are accurate
199 and extensively validated. However, due to the nature of the satellite orbit and the intermittency
200 of the revisit times, the temporal resolution of the resulting products is limited, and diurnal and
201 sub-diurnal variations cannot be captured. On the other hand, sensors onboard geostationary
202 satellites (e.g., GOES) remain in fixed positions overlooking the Earth, providing full disk

203 observations every 10 minutes. Geostationary satellites also provide increased robustness to
204 cloud coverage (Duffy et al., 2022; Hashimoto et al., 2021), a desirable feature for the study of
205 atmospheric motions generated by landscape discontinuities (F. Chen & Avissar, 1994).

206 This study introduces the Empirical Spatio-Temporal Covariance Function (ESTCF) as a
207 tool to assess the spatial coherence and memory of remotely sensed spatio-temporal fields and
208 identify patterns that might be relevant in the dynamics of processes within the SVAS.
209 Additionally, the study presents a new 4-parameter covariance model to summarize the spatio-
210 temporal structure displayed by the ESTCF and provides physical interpretations for its
211 parameters. These tools are applied to remotely sensed fields of LST to evaluate whether they
212 can identify areas where landscape features (e.g., coastlines, topographic gradients, and urban
213 areas, among others) might be responsible for triggering heterogeneity-driven atmospheric
214 circulations. These developments are implemented and tested over CONUS by splitting the
215 entire country into a mosaic of $1.0^\circ \times 1.0^\circ$ domains, deriving the summer day-time surface
216 temperature ESTCF for each domain independently, and fitting the parametric covariance model
217 to each specific domain. Once covariance functions for all domains are known, clustering
218 analysis is applied to the obtained parameter maps in order to detect areas with similar spatio-
219 temporal surface temperature dynamics. Finally, we present a combined metric for quantifying
220 the local spatio-temporal variability based on normalized values of the covariance parameters.
221 The key developments in this study include (a) a flexible and comprehensive tool to characterize
222 and represent the spatio-temporal dependence structure of remotely sensed fields, (b) a
223 parametric covariance function model to more concisely describe the spatio-temporal patterns
224 captured with the ESTCF, and (c) a multi-dimensional clustering approach to determine areas
225 with similar spatio-temporal dependence structures. The tools introduced here provide a pathway
226 forward to formally identify and summarize the spatio-temporal patterns observed in remotely
227 sensed fields and relate those to the footprint of more complex dynamic processes within the
228 SVAS.

229 **2 Data and Methods**

230 **2.1 GOES-16 LST and Sea Surface Temperature (SST)**

231 The NOAA's Geostationary Operational Environmental Satellites (GOES) are the latest
232 and main operational geostationary weather satellites in orbit over the Western hemisphere
233 (Desai et al., 2021). Recently, the GOES-R Advanced Baseline Imagers (ABIs) on board the new
234 generation GOES-16 and GOES-17 satellites have been generating an LST operational product
235 based on scans at roughly 5 minutes with an approximate 2 km spatial granularity over the
236 continental United States (CONUS). The GOES ABI LST estimates are produced using a
237 thermal channel split-window retrieval based on the bands centered at 10.8 and 12.3 μm with
238 high surface emission and low atmospheric absorption. Additionally, the algorithm uses a
239 prescribed surface emissivity and an atmospheric radiative transfer model. For further details on
240 the retrieval algorithm, the reader is referred to (Yu & Yu, 2020). The final operational product
241 has been generated at an hourly time scale from May 2017 to the present. Evaluations have
242 shown that the product is high quality, with validation studies indicating an approximate
243 accuracy of 1.5K (Chang et al., 2021; Desai et al., 2021; Yu et al., 2012).

244 Figure 1 shows two locations over CONUS and the temporal evolution of the retrieved
245 GOES-16 LST over several daytime hours in the summer. The figure demonstrates how GOES-

246 16 LST data can capture differential heating of the surface due to landscape features (e.g.,
247 mountains and lakes in domain 1 and urban areas in domain 2) with relatively high frequency.
248 Additionally, it demonstrates how the spatial and temporal evolution of LST is heavily site-
249 specific. Given the characteristic spatial and temporal scales reported for mesoscale
250 heterogeneity-driven circulations, it is expected that GOES-16 provides an observational source
251 with both sufficiently high spatial resolution (i.e., ~2km over CONUS) and high temporal
252 resolution (i.e., one hour) to perform the subsequent analyses.

253 A Sea Surface Temperature (SST) product is also produced from the ABI retrievals on
254 board the GOES satellites. The ABIs on board GOES-16 and 17 offer improved capabilities for
255 SST retrievals, over its predecessors, including five narrow bands that can be used to estimate
256 SST. Other advantages include accurate sensor calibration, image navigation and co-registration,
257 spectral fidelity, and sophisticated preprocessing. Using this information, the Level 2
258 Preprocessed (L2P) SST product is derived at the native sensor resolution (2 km at nadir,
259 degrading to 15 km at view zenith angle, 67°) using NOAA Advanced Clear-Sky Processor for
260 Ocean (ACSPO) system (Ignatov et al., 2019). SST is derived from the original 10-minute full-
261 disk brightness temperatures using the ACSPO clear-sky mask (Petrenko et al., 2010) and the
262 Non-Linear SST algorithm (Petrenko et al., 2014). Four (4) longwave bands centered at 8.4,
263 10.3, 11.2, and 12.3 μm are used. The regression is calibrated against quality-controlled in situ
264 SST observations from drifting and tropical mooring buoys in the NOAA iQuam system (Xu &
265 Ignatov, 2014). Finally, the 10-minute full-disk data is unified in time to produce the 1-hour L2P
266 product, with improved coverage and reduced cloud leakages and image noise, compared to each
267 10-minute image.

268 To explore the spatio-temporal patterns of remote sensing land surface temperature that
269 can lead to the development of heterogeneity-driven atmospheric circulations, coastal regions are
270 relevant (e.g., land-sea breezes are one of the most evident examples of an increased land-
271 atmosphere coupling strength). In this sense, a LST product alone is insufficient to perform the
272 analysis; an SST product must also be used. For this study, the hourly GOES-16 LST data over
273 CONUS is superimposed to the hourly GOES-16 SST data over the Americas region from
274 January 2018 to December 2022. The resulting 1-hour, 2-kilometer, CONUS-wide surface
275 temperature dataset is then bounded to only consider pixels containing at least 30% of land in
276 their area. This dataset is then used to determine the spatio-temporal dependence structure of the
277 LST fields in different domains. The obtained structures are expected to show consistent
278 behaviors in places where landscape features can contribute to generating heterogeneity-driven
279 circulations. We acknowledge that differences in the algorithms used to retrieve SST and LST
280 might generate inconsistencies in the values between water and land in the consolidated LST
281 dataset. However, the main reason for merging the data is to analyze the contrasting temperatures
282 in coastal patches that would be impossible to analyze using an LST product alone.

283 It is well established that atmospheric motions influenced by landscape discontinuities
284 develop mainly during summer daytime hours and are optimum under clear sky conditions (F.
285 Chen & Avissar, 1994). For this reason, analyses in this study use only warm months (i.e., June,
286 July, August, and September), daytime hours, and clear-sky pixels of the LST dataset. Daytime
287 hours are determined locally for each individual domain over CONUS (see Section 2.2) as the
288 period between two (2) hours after sunrise and two (2) hours before sunset. The raw GOES-LST

289 and GOES-SST datasets are provided in the native ABI fixed grid coordinates; therefore,
290 reprojection to the WGS84 projection (i.e., EPSG:4326) is implemented before further analyses.

291 2.2 Moving Window Sampling

292 A sliding window approach is applied to the constructed LST dataset over CONUS to
293 deal with the inherent limitations of the stationarity assumption of the selected geostatistics
294 method. The approach works by first defining a domain of size $1.0^\circ \times 1.0^\circ$ and then moving it
295 over the remotely sensed field by a distance of 0.25° in the vertical and horizontal directions, as
296 shown in Figure 2b. The $1.0^\circ \times 1.0^\circ$ box size is determined as a typical resolution used in ESMS
297 and General Circulation Models (GCMs). For each position of the box, the whole spatio-
298 temporal field of observations over summer daytime is retrieved. By adopting this approach, a
299 comprehensive analysis is performed as different combinations of landscape features are
300 considered, and it can be assumed that the stationarity assumption holds if LST is characterized
301 as approximately homogeneous within the subregions. Results obtained in the following steps
302 are also expected to be smooth due to the approach. Figure 2a shows the study domain used over
303 CONUS. The central 0.25° of each $1.0^\circ \times 1.0^\circ$ squared box obtained from the sliding window
304 approach is presented as the grid. Coordinates every 5° are shown to aid in georeferencing.

305 2.3 Empirical Spatio-Temporal Covariance Function - ESTCF

306 The summer, daytime empirical spatio-temporal covariance function (ESTCF) of LST is
307 computed for $1.0^\circ \times 1.0^\circ$ domains across the country (see Section 2.2 for details on the domain
308 definition). The objective is to summarize and characterize the spatio-temporal dynamics of the
309 LST fields in domains across the country.

310 The ESTCF expresses how the linear statistical dependence of two measurements in a
311 spatio-temporal random field reduces as the distances (in space and time) between them increase,
312 up to the lengths of statistical independence where a relation no longer exists and the covariance
313 tends to zero (Cressie & Wikle, 2015; Mälicke et al., 2020). The spatio-temporal dependence
314 structure displayed by the observed realizations is summarized using the ESTCF. The
315 mathematical procedure used to compute the ESTCF for a random field is presented next and
316 explained based on (Montero et al., 2015).

317 Let $Z(\cdot, \cdot)$ be an intrinsically stationary process observed on a set of n spatio-temporal
318 locations $\{(s_1, t_1), \dots, (s_n, t_n)\}$ where s_i is the spatial location and t_j the observation time. The
319 classical alternative to estimate the empirical covariance function using the observed values if
320 the process is second-order stationary is proposed by (Matheron, 1989). This classical estimation

321 is obtained by implementing the Method-of-Moments estimator (MoM), which for the
 322 covariance function takes the form:

$$\hat{C}(h(l), \tau(k)) = \frac{1}{\#N(h(l), \tau(k))} \sum_{\substack{(s_i, t_i), (s_j, t_j) \\ \in N(h(l), \tau(k))}} (Z(s_i, t_i) - \bar{Z}_{t_i}) (Z(s_j, t_j) - \bar{Z}_{t_j}) \quad (1)$$

323 Where $\bar{Z}_i = \frac{1}{n} \sum_m Z(s_m, t_i)$ is an estimator of the mean μ_i of the random field for the time
 324 t_i and $N(h(l), \tau(k)) = \{(s_i, t_i), (s_j, t_j) : s_i - s_j \in T(h(l)), t_i - t_j \in T(\tau(k))\}$, with $T(h(l))$
 325 being a tolerance region on \mathbb{R}^d around $h(l)$, $T(\tau(k))$ being a tolerance region on \mathbb{R} around $\tau(k)$,
 326 and $\#N(h(l), \tau(k))$ the number of different elements in $N(h(l), \tau(k))$, with $l = 1, \dots, L$ and
 327 with $k = 1, \dots, K$.

328 In general, the areas $T(h(l))$ and $T(\tau(k))$ are chosen to yield disjoint sets with enough
 329 elements to generate stable estimates (i.e., domain sizes with enough observations to generate an
 330 adequate estimation of the ESTCF). Suppose the hypothesis of isotropy is reasonable for the
 331 spatial process under analysis. In that case, the area of spatial tolerance around each of the values
 332 $h(l)$ can be defined as $[h(l) - d_l/2, h(l) + d_l/2]$, with d_l being the spatial tolerance to be
 333 used. Also common is to make the temporal component take values in \mathbb{Z} , in which case the
 334 empirical covariance function is computed for $\tau(k) = 0, 1, \dots$, obtained as the subsequent
 335 differences in time at which the process is observed. To better illustrate the described procedure,
 336 a simplified example is included next.

337 Let us suppose there is a set of spatio-temporal measurements taken in three (3)
 338 moments, t_1, t_2 , and t_3 , on a regular grid of size 3×3 with a spacing of 2 kilometers (Figure 3a).
 339 Assuming the resulting spatio-temporal random field is isotropic and stationary and that
 340 tolerance regions are not used, the classical ESTCF will be given by the simplified form of
 341 Equation 1:

$$\hat{C}(h, \tau) = \frac{1}{\#N(h, \tau)} \sum_{N(h, \tau)} (Z(s_i, t_i) - \bar{Z}_{t_i}) (Z(s_j, t_j) - \bar{Z}_{t_j}) \quad (2)$$

342 In this example, it is easy to show that there are $9 \times 3 = 27$ spatio-temporal points at a
 343 distance $(h, \tau) = (0km, 0)$. Therefore, for Equation 2, $\#N(h, \tau) = 27$. By definition, $\hat{C}(0km, 0)$
 344 is the spatio-temporal variance of the random field, σ^2 .

345 Suppose the distance is $(h, \tau) = (0km, 1)$, then $\#N(h, \tau) = 9 \times 2 = 18$. Finally, if the
 346 distance is $(h, \tau) = (0km, 2)$, $\#N(h, \tau) = 9 \times 1 = 9$. If the empirical covariance is computed
 347 for all the previously defined spatio-temporal distances, the purely temporal empirical covariance
 348 function is obtained (i.e., only time varies). It is also trivial to prove that: $\#N(2km, 0) =$
 349 $12 \times 3 = 36$ and $\#N(4km, 0) = 6 \times 3 = 18$. If the empirical covariance is computed just for
 350 the distances $(h, 0)$, the purely spatial empirical covariance is obtained. Additionally, cases
 351 where both the spatial and temporal lags are different from zero, can also be considered, though

352 the pairs of points must be determined carefully. For instance, Figure 3b shows the 12 pairs of
353 points separated by a spatio-temporal distance $(h, u) = (4km, 2)$. It is important to mention that
354 this procedure does not consider diagonal spatial distances for simplicity.

355 Since the produced LST dataset already uses a regular spatio-temporal grid, the
356 procedure described for the example is directly applied. As mentioned before, only clear sky,
357 summer daytime pixels are used for the analysis. If one or both points contained in any pair used
358 to compute the ESTCF contain a missing value, the pair is ignored from the summation in
359 Equation 2, and $\#N$ is modified accordingly by subtracting one. Additionally, to determine the
360 spatial separation between points, h , each pixel is assigned its central coordinates in degrees..

361 Two conditions are implemented regarding the spatial distribution and number of missing
362 values of the LST dataset within each domain for every time step: i) the average latitude and
363 longitude of the LST valid pixels within the domain has to be within a range of $\pm 0.15^\circ$ of the
364 central latitude and longitude of box; otherwise, the time step LST values for the domain are
365 considered missing and; ii) the fraction of missing LST values within each domain per time step
366 cannot be higher than 0.25; otherwise, the time step values are considered missing. Finally, some
367 ESTCF results presented in the following sections are normalized by the spatio-temporal
368 variance of the field over the local domain (σ^2), as a way to make results comparable and
369 analyze differences beyond the magnitude of the spatio-temporal variance.

370 2.4 A Parametric Model for the Spatio-Temporal Covariance Function

371 Once the ESTCF is computed for every domain in CONUS, a parametric model is fitted
372 to it, and the obtained parameters are used to determine the similarity in the spatio-temporal
373 dependence structures between domains.

374 Typically, the end goal when estimating the ESTCF of a random field is to use the
375 information contained within the observations to perform prediction of values for unobserved
376 locations (i.e., spatio-temporal kriging prediction or modeling). In such cases, a positive definite
377 covariance function is a requirement to define a valid stochastic process. However, the spatio-
378 temporal dependence structure derived from observations (i.e., ESTCF) usually does not fulfill
379 the condition of being positive-definite. For this reason, in practice, a parametric model of
380 covariance that is already known to be valid is selected and fitted to the ESTCF. An extensive
381 body of literature deals with proper covariance models for spatio-temporal prediction. For a
382 comprehensive review of these models, the reader is referred to (Cressie & Huang, 1999; Cressie
383 & Wikle, 2015; Montero et al., 2015; Stein, 2005). Two main types of theoretical spatio-
384 temporal covariance models exist: separable and non-separable. Separable models are built using
385 the sum or product of a purely spatial and purely temporal covariance, both stationary. In this
386 sense, separable models do not consider interactions between space and time in the dependence
387 structure of the field. Non-separable models, on the other hand, capture the space-time
388 dependence that exists on most phenomena by including the interaction between the two
389 dimensions.

390 For this study, the end goal is not predicting LST at ungauged locations but rather the
391 characterization of the spatio-temporal dynamics of the LST fields. In this sense, the positive-
392 definite nature of the selected parametric model is not a requirement. However, it is desirable

393 that the chosen model uses a small set of parameters and that each is physically meaningful. For
 394 this reason, a modified form of the non-separable parametric model presented by (Cressie &
 395 Huang, 1999) is selected:

$$C(h, u) = \sigma^2 e^{-\left(\frac{\tau^a}{\gamma}\right) - \left(\frac{h^a}{\lambda}\right)} \quad (3)$$

396 Where $C(h, u)$ is the parametric covariance at a spatio-temporal distance (h, u) ; σ^2 is the
 397 spatio-temporal variance of the random field, computed directly from the data; γ is the fitted
 398 temporal characteristic length-scale; λ is the fitted characteristic spatial length-scale; and a is the
 399 fitted spatio-temporal interaction exponent. Several other parametric models were tested on the
 400 available data, but the one selected showed improved performance with the lowest number of
 401 parameters.

402 2.5 Impact of the Parameters in the Spatio-Temporal Covariance Parametric Model

403 In the selected model, the space-time interaction exponent (a) determines the shape of the
 404 space-time interaction, while the characteristic length scales (i.e., γ and λ) modify the magnitude
 405 of the spatial and temporal distances after they have been affected by the exponent. Figure 4
 406 displays the spatio-temporal covariance functions obtained as the values of the parameters are
 407 successively modified. The figure allows us to see how:

- 408 • Larger values of the characteristic temporal length scale, γ , result in higher memory (see
 409 Figure 4c). In other words, for the produced parametric model, high covariance values are
 410 bound to persist longer in time as γ increases. When fitted to an observational dataset, a
 411 high value of γ implies that the variable patterns tend to remain for longer for the
 412 location. The opposite behavior (i.e., shorter persistence) can also be achieved by
 413 reducing γ , as observed in Figure 4a.
- 414 • Increased spatial persistence of the modeled covariance function is achieved by raising
 415 the spatial length scale, λ (see Figure 4f). A fitted high λ suggests a significant extent of
 416 the spatial patterns in the domain. In that case, the values of the observations for two
 417 points far from each other are highly correlated. The contrasting case (i.e., smaller spatial
 418 patches of values) can be modeled by decreasing λ , as presented in Figure 4d.
- 419 • Higher values of the space-time interaction exponent, a , lead to an increased interaction
 420 between space-time in the computed covariance function. The space-time interaction is
 421 directly related to the shape of the curves in the modeled covariance function. As a rises
 422 over one (see Figure 4i), the interaction between space and time becomes stronger, and
 423 the modeled transition between the pure-spatial and pure-temporal covariance occurs by
 424 displaying a convex shape. The opposite case (i.e., $a < 1.0$) generates a concave shape in
 425 the transition between pure-spatial and pure-temporal covariance, as seen in Figure 4g.
 426 Additionally, due to the function structure, the modeled memory and spatial coherence
 427 emulated by the parametric model are also directly influenced by the magnitude of the
 428 spatio-temporal interaction exponent, a . In each dimension, the presence of the exponent
 429 determines a stretched exponential shape for the correlation function, which encompasses

430 longer tails ($a < 1.0$) or shorter tails ($a > 1.0$) compared to a simple exponential, while
 431 retaining a characteristic scale (Laherrère & Sornette, 1998).

432 In general, it is expected that once applied to the LST dataset, domains with high values
 433 of the two characteristic length-scale parameters and the space-time interaction exponent (i.e., a
 434 over 1) display the coherent memory associated with the initiation of heterogeneity-driven
 435 circulation systems.

436 Additionally, modified forms of the spatial and temporal characteristic length scales can
 437 be derived to obtain an approximation unaffected by the spatio-temporal interaction exponent
 438 and identify the individual effects of space and time on the joint spatio-temporal dynamics.
 439 These forms are estimated as the fitted characteristic length scales operated by the fitted spatio-
 440 temporal interaction exponent, as displayed in Equations 4 and 5.

441

$$\gamma' = \sqrt[a]{\gamma} \quad (4)$$

$$\lambda' = \sqrt[a]{\lambda} \quad (5)$$

442

443 To fit the ESTCFs to the parametric model, non-linear least squares regression is used.
 444 The function is set up to use the Trust Region Reflective method, TRF, to perform the
 445 minimization. The TRF method is particularly suitable for large sparse problems with bounds,
 446 and it is generally robust. Based on an analysis of the selected function, the bounds for the
 447 parameters to be fitted are defined as $0 < \gamma \leq 100$, $0 < \lambda \leq 10$, and $0.5 < a \leq 3$.

448 2.6 Clustering Analysis

449 Once the parametric model is fitted to the ESTCFs, an unsupervised clustering algorithm
 450 determines zones with relatively homogeneous parameter values. Such spatial clustering has
 451 been used to map zones that represent co-varied features in a tractable manner (e.g., (Devadoss et
 452 al., 2020; Wainwright et al., 2022)). In this case, the identified clusters are anticipated to
 453 comprise areas with consistent potential for land-atmosphere circulations.

454 The commonly used k-means method is selected as a clustering algorithm. The features
 455 used to perform the clustering are the fitted spatio-temporal characteristic length scales and
 456 interaction exponent, as well as the spatio-temporal variance computed directly from the LST
 457 data. Each feature is normalized by its minimum and maximum values before performing the
 458 clustering. The dissimilarity between two data points is determined based on the Euclidean
 459 distance. To determine the appropriate number of clusters to use, the elbow method is adopted.
 460 In the elbow method, k-means clustering is performed on the dataset for a range of k values (i.e.,
 461 number of clusters). Then, for each k, the method computes an average score for all clusters. By
 462 default, the distortion score is computed. The distortion scores the sum of square distances from
 463 each point to its assigned center in the clustering. Once this metric for k is plotted, it is possible
 464 to visually determine the best value for the number of clusters, as the k where the inflection point
 465 of the curve occurs. Using the obtained number of clusters, k-means is applied, and the resulting
 466 clusters are mapped out and analyzed in terms of their characteristic spatio-temporal covariance

467 function (CSTCF), which for each cluster is computed using the parametric model with the mean
 468 value of all the domains contained within the same cluster.

469 2.7 Combined metric for spatio-temporal persistence

470 The tools developed in this study pave the way to using solely remote sensing
 471 information to detect areas characterized by homogeneous spatio-temporal dynamics. This
 472 information can, in turn, be employed to investigate which landscape features can be linked to
 473 heterogeneity-driven circulations. To this end, we construct a metric (m) based on normalized
 474 values of the parameters of the fitted spatio-temporal covariance function. Rescaled forms of the
 475 model parameters are used as performance metrics for each component of the spatio-temporal
 476 dependence structure. After normalization, parameter values range from zero (low spatio-
 477 temporal variability score) to one (high spatio-temporal variability score). Equations 6 to 9
 478 present the computation of the rescaled forms for each parameter. Capital variables (i.e., Σ^2 , Γ , Λ ,
 479 and A) represent the CONUS broad fields of parameters, while lowercase variables (i.e., σ^2 , γ ,
 480 λ' , and a) designate the domain or cluster of domains specific parameter values.

$$\sigma_{rs}^2 = \frac{\sigma^2 - \min(\Sigma^2)}{\max(\Sigma^2) - \min(\Sigma^2)} \quad (6)$$

$$\gamma_{rs} = \frac{\gamma - \min(\Gamma)}{\max(\Gamma) - \min(\Gamma)} \quad (7)$$

$$\lambda_{rs} = \frac{\lambda - \min(\Lambda)}{\max(\Lambda) - \min(\Lambda)} \quad (8)$$

$$a_{rs} = \frac{a - \min(A)}{\max(A) - \min(A)} \quad (9)$$

481 Once all the parameters are rescaled, the combined metric (m) for each domain or cluster
 482 of domains can be computed as shown in Equation 10. This combined metric takes values
 483 between zero (0) for locations with minimum spatio-temporal persistence to four (4) for areas
 484 with maximum spatio-temporal persistence.

$$m = \sigma_{rs}^2 + \gamma_{rs} + \lambda_{rs} + a_{rs} \quad (10)$$

485 3 Results

486 3.1 ESTCF over CONUS

487 The summer daytime ESTCFs over CONUS were computed using all the available LST
 488 observations according to the procedure described in Sections 2.2 and 2.3. The obtained ESTCFs
 489 for seven (7) locations with various landscape features are presented in Figure 5. The figure
 490 shows the site-specificity of the obtained ESTCFs. As expected, the spatio-temporal variance of
 491 LST (i.e., the maximum value of the color bar) was higher for mountainous areas (i.e., Colorado
 492 and Lake Tahoe, Figures 5b and 5c), and for coastal regions, including lake coastlines (i.e., New
 493 York City and Lake Michigan, Figures 5f and 5g), due to contrasting landscape features such as
 494 topography and material thermal properties. The observed variance values for flat areas were

495 relatively low, with values around $3K^2$ for the Louisiana, Atlanta, and North Dakota domains
 496 (Figures 5d, 5e, and 5h).

497 It was observed that the contrast between land cover types, particularly water vs. land,
 498 increased the space-time interaction by producing a convex transition between space and time in
 499 the ESTCFs. The same convex transition was observed for mountainous regions (Figures 5b and
 500 5c). Additionally, domains containing features such as rivers, cities, and small lakes (Figures 5d,
 501 5e, and 5h), which had generally homogeneous landscapes except for the small-scale features
 502 (i.e., in the order of 10-30km), displayed a relatively sharp decay in their spatial coherence.
 503 Domains displaying large-scale heterogeneity, driven by topography or contrasting land cover
 504 (especially land vs. water), showed larger spatial coherences (see Figures b, c, f, g).

505 Regarding the temporal persistence (i.e., memory) of the ESTCFs in the analyzed
 506 domains, it was observed that the presence of large-scale landscape features, such as bodies of
 507 water and topographic gradients, increased the temporal persistence of the ESTCF. The domains
 508 with the longer persistence of summer daytime LST were the ones located in Colorado (~5hr,
 509 Figure 5c), California (~4hr, Figure 5b), and New York City (~2.5hr, Figure 5f). Smaller
 510 persistence values, in the order of 1hr, were detected for all the other domains.

511 3.2 Spatio-Temporal Covariance Function: Parametric model over CONUS

512 Once the ESTCFs were computed for CONUS, the selected parametric model for the
 513 spatio-temporal covariance function was fitted to them, as described in Sections 2.4 and 2.5. The
 514 obtained parametric fits for the seven (7) domains analyzed in Figure 5 are presented in Figure 6.
 515 For the locations of the domains over CONUS, the reader is referred to Figure 5a.

516 Figure 6 shows the performance of the selected parametric model in reproducing the
 517 observed ESTCFs. The Figure displays zoomed-in satellite imagery for each domain, the
 518 ESTCFs computed from the LST observations, the obtained fit, the set of parameters
 519 corresponding to that fit, and the normalized root mean square error (nRMSE) as a performance
 520 metric. Visual inspection showed that, in general, the parametric model performed well for the
 521 selected locations, particularly for the higher covariance values on the bottom left part of the
 522 spatio-temporal domains, $0.7 \leq C/\sigma^2 \leq 1.0$. This was expected, as these values played a more
 523 critical role in the normal least squares minimization algorithm used in the fit. The obtained
 524 nRMSE values confirmed the results derived from the visual inspection. Higher nRMSE values
 525 were observed for domains with larger spatio-temporal variance values (i.e., mountainous
 526 domains and coastal domains; Figures 6a, 6b, and 6e). This behavior can be explained by the fact
 527 that the selected model was overly simplistic to represent the complex space-time interactions
 528 that could emerge in some regions.

529 Regarding the magnitude of the obtained parameters, it was clear that domains where
 530 interactions between land and water existed (Figures 6e and 6f) and where significant
 531 topographic gradients were present (Figures 6a and 6b) displayed higher values of the temporal
 532 characteristic length-scale, γ , and values of the spatio-temporal interaction exponent, a , over 1.
 533 For the remaining domains (Figures 6c, 6d, and 6g), the spatial characteristic length-scale, λ ,
 534 seemed to play a more critical role in reproducing the ESTCF, with relatively high values.

535 Additionally, for these cases, the spatio-temporal interaction exponent, a , kept values slightly
 536 under or over 1.0, indicating an almost linear spatio-temporal interaction.

537 The fit to the parametric spatio-temporal covariance function model was performed for
 538 every $1.0^\circ \times 1.0^\circ$ domain under analysis with at least 2/3 of its area over land. Figure 7 presents
 539 the integrated results for this procedure as maps. Each pixel represents the central $0.25^\circ \times 0.25^\circ$
 540 for each $1.0^\circ \times 1.0^\circ$ analyzed domain. Maps for the fitted spatio-temporal characteristic length
 541 scales, γ and λ , are presented (Figures 7b and 7c), as well as for the fitted spatio-temporal
 542 interaction exponent, a , (Figure 7d) the computed spatio-temporal variance, σ^2 , (Figure 7a) and
 543 the nRMSE obtained for the fit (Figure 7e). It is worth mentioning that the ESTCFs presented in
 544 Figure 5 and Figure 6 did not share the same time lag axis limits due to the location-dependent
 545 day lengths. However, the temporal lag axis was standardized for the CONUS-wide fit, $0 \leq \tau \leq$
 546 $8hr$. The results reveal:

- 547 1. Spatio-temporal variance (Figure 7a): A West to East decreasing gradient of variance was
 548 observed, showing agreement with the long-term precipitation climatology for the area.
 549 Additionally, the obtained gradient was also consistent with the Köppen-Geiger climate
 550 classification system for CONUS, with drier climates displaying a larger LST variability
 551 with a lower influence of surface soil moisture content. As expected, higher variance
 552 values were observed in regions with significant topographic gradients, coastlines, urban
 553 areas, particularly in the Midwest and the Mississippi River delta area in Louisiana.
 554 Coastal areas of the Atlantic and Pacific showed clear differences, with the Pacific coast
 555 displaying larger variance values due to a sharper contrast in temperature between land
 556 and water. The lowest values were located in flat areas in the central and eastern regions
 557 of CONUS.
- 558 2. Temporal characteristic length-scale (Figure 7b): The observations derived from Figure 6
 559 were confirmed in this case with increased values of γ in mountain areas and coastal
 560 regions, particularly in the Sierra Nevada, Rocky Mountains, Coastal ranges,
 561 Appalachians, California Gulf, Northeast coastlines and Great Lakes shorelines. Urban
 562 areas in the Midwest, South, and Northeast also showed elevated values in comparison to
 563 their surroundings.
- 564 3. Spatial characteristic length-scale (Figure 7c): An east-to-west decreasing gradient for
 565 this parameter was observed. Higher values were identified for flat areas of the Midwest.
 566 Unlike the temporal characteristic length scale, urban sites, coastlines, and mountain
 567 ranges displayed reduced values, probably due to a heavy influence of the spatio-
 568 temporal interaction exponent.
- 569 4. Spatio-temporal characteristic length-scale (Figure 7d): The patterns observed here
 570 resemble the ones for the spatio-temporal variance (Figure 7a). Concave spatio-temporal
 571 interactions ($a < 1$) were found in flat areas of the South, non-coastal areas of the
 572 Midwest, and non-urban portions of the Northeast. Linear relationships between space
 573 and time ($a \cong 1$) were identified for urban areas of the Midwest and South, as well as in
 574 relatively homogeneous domains in the West. In general, domains containing coastlines

575 and significant topographic gradients consistently displayed a convex spatio-temporal
576 interaction ($a \geq 1$).

577 5. nRMSE (Figure 7e): The model struggled to thoroughly capture the observed dynamics
578 in the Appalachians, Sierra Nevada, Rocky Mountains, Coastal ranges, and some urban
579 areas of the Midwest and Northeast. However, due to the general performance, it was
580 concluded that the selected parametric model represented the spatio-temporal dynamics
581 of LST in a relatively accurate way, with a CONUS-wide mean nRMSE of $\sim 3\%$.

582 Alternative forms of the length scales were derived to obtain an approximation unaffected
583 by the spatio-temporal interaction exponent and identify the individual effects of space and time
584 on the joint spatio-temporal dynamics. These forms were estimated as the fitted characteristic
585 length scales operated by the fitted spatio-temporal interaction exponent (as described in Section
586 2.5). Another goal of this procedure was to identify locations where the spatial characteristic
587 length-scale displayed patterns that could not be placed directly from Figure 7. Figure 8 shows
588 the maps of the alternative forms of the spatio-temporal characteristic length scales with units. In
589 general, the modified temporal characteristic length-scale (Figure 8a) displayed some of the
590 same patterns identified using Figure 7b: increased values in mountainous areas and urban zones
591 in the Midwest, South, and Northeast with elevated values compared to their surroundings. For
592 mountainous regions, the magnitude of the modified temporal scale (i.e., memory) was in the
593 range of 20 to 60 hours (i.e., one day to 2.5 days). For the urban areas cases, the obtained
594 memory was on the order of 10 hours. However, unlike Figure 7b, Figure 8a showed that the
595 contrast between land-only domains and coastal domains, particularly in the California Gulf, the
596 Great Lakes shorelines, and the Northeast coastline, was not as high for the modified temporal
597 characteristic length-scale, with memories slightly below 10 hours. This implies that the
598 increased values of γ in these locations were caused by an elevated space-time interaction
599 exponent rather than by a time-only effect. On the other hand, the modified spatial characteristic
600 length-scale (Figure 8b) displayed increased values in domains with persistent landscape
601 features, including coastlines and mountain ranges, a pattern expected but not observed on the
602 original spatial characteristic length-scale map (Figure 7c). In this sense, for these locations, the
603 spatio-temporal interaction parameter reduced the influence of the space-only characteristic
604 length-scale, probably due to the magnitude of the distances (below 1°).

605 3.3 Clustering analysis

606 With all the parameter values from the model fit, an unsupervised clustering algorithm
607 (i.e., k-means) was used to identify homogeneous zones. The number of clusters to be used (i.e.,

608 k=6) was determined using the elbow method based on the distortion score, as displayed in
 609 Figure 9a.

610 Figure 9b presents the location of the obtained clusters over CONUS. The resulting
 611 clustered regions are described below:

- 612 • **Cluster 1** occupied 41.17% of the total CONUS area, and it corresponded mainly to flat
 613 spots in the Midwest and Atlantic coastal plain regions, with some low zones on the
 614 Mountain and Pacific West.
- 615 • **Cluster 2** covered the smallest area (1.09% of the total CONUS area) and grouped
 616 domains containing the coastal regions of the Gulf and South of California and the
 617 Central Valley coastline.
- 618 • **Cluster 3** occupied 7.75% of the total area and included mostly transitional domains next
 619 to significant topographic gradients (e.g., Sierra Nevada, Rockies, Coastal ranges, Black
 620 Hills, and Appalachians), as well as some coastal or semi-coastal regions in the
 621 Northeast, the Great Lakes shorelines (except for the Lake Erie coastline, probably due to
 622 its relatively small size), the Great Salt Lake area, and the Gulf of California.
- 623 • **Cluster 4** was the second largest region, with 30.84% of the total area, and contained
 624 most of the Central region of the US, as well as most of the coastline domains in the Gulf
 625 of Mexico and Southeastern US, and domains including large urban areas of the Midwest
 626 and South (e.g., Nashville, Memphis, Saint Louis, Kansas City, Indianapolis, Chicago,
 627 Milwaukee, among others). A significant portion of the Appalachian Mountains with
 628 intermediate elevations was also included in Cluster 4.
- 629 • **Cluster 5** occupied 15.10% of the total area and primarily encompassed low regions of
 630 the Western US, including the California Central Valley, as well as flat areas of Nevada,
 631 Arizona, Utah, and Baja California in Mexico; it also included some coastal domains,
 632 mainly in the Lake Erie area, as well as Northern parts of Lake Michigan, and Eastern
 633 coasts of Lake Huron. The Chesapeake Bay area in Maryland and some domains in the
 634 Appalachian region were also included in Cluster 5.
- 635 • **Cluster 6**, occupying 4.05% of the total CONUS area, contained all the domains with the
 636 highest elevations of the Sierras, Coastal Ranges, Rockies, Appalachians, and Lake
 637 Superior shorelines.

638

639 Figure 10 presents the spatial mapping of the clusters over CONUS, as well as the
 640 parametric representation of the spatio-temporal covariance function obtained from the mean
 641 cluster value of the parameters (i.e., the mean value of the parameter values for all the domains
 642 contained within the same cluster) or characteristic spatio-temporal covariance function (CSTCF).
 643 The first observation derived from Figure 10 is the variance discrimination between groups. In
 644 general, locations with higher variances, $\overline{\sigma^2}$, (i.e., Pacific coast and Gulf of California, higher
 645 elevations of Rockies, Sierra, Coastal ranges and Appalachians, and shorelines of Lakes Superior,
 646 Michigan, Huron, and Ontario) were grouped by the clustering procedure in Cluster 2, Cluster 6,

647 and Cluster 3, respectively (Figures 10b,10f, and 10c). Due to the topographic and material
 648 contrast within those high variance domains, the obtained shape for the CSTCF was predominately
 649 convex with mean exponent values \bar{a} over one, particularly in the Cluster 2 case. That was also
 650 the case for the mean characteristic temporal length-scale, $\bar{\gamma}$, with the highest values associated
 651 with the larger variance clusters. Due to the previously discussed influence of the spatio-temporal
 652 interaction exponent, the mean characteristic spatial length-scale results were less clear. As for the
 653 lower variance clusters, Cluster 1, Cluster 4, and Cluster 5 (Figures 10a, 10d, and 10e,
 654 respectively), each exhibited distinctive characteristics. Besides presenting the lowest $\bar{\sigma}^2$ values,
 655 Cluster 1 displayed low values of $\bar{\gamma}$ and \bar{a} (i.e., concave shape). Cluster 4 featured the second
 656 lowest variance with an almost linear space-time interaction exponent, \bar{a} , and relatively low $\bar{\gamma}$.
 657 Finally, Cluster 5 constituted a transitional group with the third lowest variance but relatively high
 658 values of both \bar{a} and $\bar{\gamma}$.

659 The box plots in Figure 11 display the distribution of parameter values within each cluster
 660 and aid in identifying the main factors determining the grouping. Cluster 1 was mainly controlled
 661 by the lowest a and γ values and the highest λ ; Cluster 2 by the highest γ , a , and σ^2 values; Cluster
 662 3 by the second highest values of γ , and intermediate ones of a and σ^2 ; Cluster 4 by the second
 663 lowest γ and a and the second highest λ values; Cluster 5 by the third lowest γ , a , and σ^2 values;
 664 and Cluster 6 by the highest γ and the second highest λ , a , and σ^2 values.

665 3.4 Combined metric for spatio-temporal persistence

666 The combined metric for spatio-temporal persistence described in Section 2.7 was
 667 computed for every domain in CONUS. The combined metric values for each domain are
 668 presented in Figure 12a, and the individual contribution of the rescaled forms of the parameters to
 669 the total metric value in Figures 12b, 12c, 12d, and 12e.

670 In general, Figure 12a shows that domains with certain landscape features displayed
 671 increased metric values with respect to their surroundings. These features included coastlines,
 672 mountainous ranges, urban areas, and large rivers. Higher values were found in the Gulf of
 673 California coastline, Lake Superior and Michigan shorelines, Sierra Nevada, and higher elevations
 674 of the Rocky Mountains and Coastal Ranges. Lower values focused on domains within the
 675 Midwest and Atlantic coastal plain regions, excluding coastlines. Regarding the individual
 676 contributions of the parameters to the total metric value, Figure 12b showed that for most cases,
 677 the spatio-temporal variance was negligible, contributing to less than 10% of the total metric value
 678 in most locations. For the temporal characteristic length-scale displayed in Figure 12c, the
 679 contributions to the metric were higher in mountainous regions, the Southern Pacific and Northern
 680 Atlantic coastlines, and the Great Lakes shorelines, reaching values of about 40%. Figure 12d
 681 showed that the spatial characteristic length-scale contributed significantly to the metric mainly
 682 in flat domains of the Midwest and Atlantic coastal plain regions and central CONUS, with values
 683 ranging between 40% and 80%. Finally, the spatio-temporal interaction exponent (Figure 12e) was
 684 consistently high for most of the domains, with significant contributions in the Atlantic coastline,
 685 cities in the Midwest, Appalachian mountains, Great Lakes shorelines, and most of the Mountain
 686 West domains, except for the higher elevations where the temporal characteristic length-scale
 687 dominated.

688 The combined metric for spatio-temporal persistence was also computed for the mean
 689 value of the parameters obtained from clustering. Table 1 displays the combined metric for each
 690 cluster and the individual contributions of the rescaled forms of the mean parameters. Cluster 2,

691 composed of the coastal domains in the Gulf of California and the South Pacific region, resulted
 692 in the highest metric value and, therefore, a presumed highest potential for the development of
 693 land-atmosphere circulations. The increased importance of the temporal characteristic length-scale
 694 and the spatio-temporal interaction exponent mainly drove this behavior. This result pointed
 695 toward the joint effects of the temporal persistence (i.e., memory) and the spatio-temporal
 696 interaction as the main factors determining the structure of the LST fields in those domains. Cluster
 697 6 presented the second largest values of the metric, containing domains with the highest
 698 topographic gradients as well as some coastal areas in the Great Lakes region. In this case, the
 699 main driver of the metric was the temporal characteristic length-scale indicating an essential
 700 influence of the memory of the spatio-temporal structure of the fields. A moderate metric value
 701 was observed for Cluster 3 and 5, mainly driven by relatively high values of the spatio-temporal
 702 interaction exponent. Finally, Clusters 1 and 4 resulted in the lowest metric values; even though
 703 they had the highest values of the spatial characteristic length scales, low values of all the other
 704 three parameters resulted in overall reduced metric values.

705

706 **Table 1.** Mean parameter values per cluster, rescaled values of the parameters, and mean metric
 707 per cluster.

	σ^2		γ		λ		a		Metric (m)
	Mean value	Rescaled	Mean value	Rescaled	Mean value	Rescaled	Mean value	Rescaled	
Cluster 1	3.28	0.03	4.22	0.03	0.22	0.34	0.81	0.16	0.56
Cluster 2	60.80	0.52	86.31	0.86	0.09	0.13	2.20	0.88	2.40
Cluster 3	15.87	0.13	45.05	0.44	0.11	0.16	1.61	0.58	1.32
Cluster 4	5.51	0.05	9.74	0.09	0.17	0.26	1.07	0.30	0.69
Cluster 5	9.74	0.08	19.57	0.19	0.11	0.16	1.38	0.46	0.89
Cluster 6	18.67	0.16	89.89	0.90	0.12	0.18	1.73	0.64	1.87

708

709 4 Discussion

710 4.1. General implications and specific application findings

711 This study introduced the Empirical Spatio-Temporal Covariance Function (ESTCF) to
 712 evaluate the spatial coherence and memory of remotely sensed spatio-temporal fields. The main
 713 aim was to uncover significant spatio-temporal patterns within the observed processes in the
 714 Soil-Vegetation-Atmosphere System (SVAS). The proposed approach was applied to remotely
 715 sensed LST fields to determine whether the application could successfully pinpoint regions
 716 where landscape characteristics such as coastlines, topographic gradients, and urban areas might
 717 be influential in initiating heterogeneity-driven circulation systems. The procedure was
 718 implemented and assessed across the contiguous United States (CONUS). The country was
 719 divided into distinct $1.0^\circ \times 1.0^\circ$ domains. For each area, the summer day-time LST ESTCF was
 720 calculated independently, and subsequently, the parametric covariance model was fitted to the
 721 data. Following the fitting process for all domains, a clustering analysis was employed to
 722 recognize areas that share analogous spatio-temporal dynamics of LST, suggesting similar

723 potential for heterogeneity-driven circulation generation. The key contributions of this paper
724 encompassed a) introducing a versatile and comprehensive tool to depict and characterize the
725 spatio-temporal interdependence structure of remotely sensed fields, b) presenting a parametric
726 covariance function model that succinctly characterizes the spatio-temporal configurations
727 captured by the ESTCFs, and c) proposing a multi-dimensional clustering strategy to discern
728 regions with analogous spatio-temporal dependency structures. The methodology introduced in
729 this study is expected to pave the way for a systematic analysis of the spatio-temporal patterns
730 present in remotely sensed fields, as these insights can be linked to physical processes within the
731 SVAS.

732 The ESTCF was easily obtained from gridded observations and proved flexible enough to
733 deal with missing data, varying domain sizes, and differential temporal aggregations.
734 Additionally, the ESTCF displayed the ability to characterize spatio-temporal regimes based on
735 features of the fields such as spatio-temporal variance, spatial coherence structure, temporal
736 persistence, and space-time interactions. Overall, the proposed parametric model of the
737 covariance function accurately emulated the empirical data while simultaneously summarizing
738 the dynamics within the ESTCFs. The simplified features were then used to identify areas with
739 homogeneous spatio-temporal dynamics, successfully classifying domains based on their main
740 spatio-temporal features.

741 Regarding the application of the proposed methods to the LST fields, the joint use of the
742 clustering procedure and the proposed combined metric for spatio-temporal persistence allowed
743 the identification of zones with higher spatio-temporal dynamics in coastal domains of the Gulf
744 of California and the South Pacific region and domains containing the highest elevations of
745 mountainous areas (i.e., the Sierra Nevada, Rockies, Coastal Ranges, Appalachian Mountains) as
746 well as the coastal areas surrounding the largest lakes in the Great Lakes region. These locations
747 coincided with those reported in the literature to have an increased likelihood of developing
748 mesoscale heterogeneity-driven circulations. The main drivers of the increased spatio-temporal
749 variability in these locations were the temporal characteristic length-scale and the spatio-
750 temporal interaction component. These findings reinforce the essential influence of the memory
751 of the spatio-temporal structure of the fields in the presumed potential of land-atmosphere
752 coupling development. Additionally, the low individual contribution of the spatio-temporal
753 variance to the total combined metric value underlined the necessity for Earth System Models
754 (ESMs) to include more comprehensive metrics than spatially aggregated macroscale grid
755 statistics (e.g., spatial mean and variance) to inform their atmospheric components of the state of
756 their land components.

757 4.2 Limitations and implications of method choices

758 4.2.1 Issues regarding the ESTCF

759 The ESTCF was selected in this study as the tool to summarize the spatio-temporal
760 dependence structure of remotely sensed fields of LST over CONUS. The tool was chosen as it
761 is easily attainable from the available remotely sensed data, providing a relatively dense
762 characterization of the heterogeneity degree on different spatial and temporal scales. Although
763 this tool provided a promising path forward for a robust evaluation and summarization of the

764 multi-scale spatio-temporal heterogeneity in large-scale observational fields, the limitations of
765 the methodology should be considered.

- 766 1. *Sampling issues*: The accuracy of the ESTCF is highly dependent on the number of available
767 observations for the covariance computation in each spatio-temporal distance. As mentioned
768 in Section 2.1, cloud cover and atmospheric aerosols directly influence the LST retrieval
769 processes, as they can obstruct the satellite's view of the surface, leading to spatial data gaps
770 and reduced observations over time. In general, it is well known that cloudiness leads to cool
771 bias in satellite-derived LST, particularly within cloudy areas (e.g., mountainous areas).
772 Additionally, developed heterogeneity-driven circulations might lead to increased cloudiness,
773 which could negatively impact the quality of the available fields of observation in specific
774 domains. Other factors affecting the retrieval of different variables (soil moisture content,
775 snow coverage, vegetation fraction, and material differences, among others) will undoubtedly
776 impact the accuracy of the computed ESTCFs if different processes are analyzed. In this
777 sense, future work should investigate the sensitivity of the ESTCFs to the availability of
778 observations in observation-limited domains.
- 779 2. *Selection of a spatio-temporal covariance parametric model*: The selected structure for the
780 covariance function parametric model was chosen as a trade-off between the number of
781 parameters (and their physical interpretability) and an accurate representation of the data-
782 derived ESTCFs. However, this structure represents one of many possible alternatives to
783 model the spatio-temporal dynamics of geospatial fields. Research on geostatistics has
784 derived many forms for covariance models, and more are expected to be developed (Bolliger
785 et al., 2007; W. Chen et al., 2021; Gneiting, 2002; de Iaco, 2010; Ma, 2003; Schepanski et
786 al., 2015). The selected function imposes a specific a priori structure to the spatio-temporal
787 dependence that might not be appropriate for all domains, variables, time aggregations, or
788 applications (e.g., not all domains or variables would benefit from a non-separable,
789 exponential parametric model). Consequently, further investigations should apply the ideas
790 exposed throughout this study to other spatio-temporal covariance parametric models in
791 order to determine the most appropriate version of it. Nonstationary covariance structures
792 could be evaluated for specific processes as it is expected that, in some cases, the covariance
793 structure may change in response to physical changes in the equilibrium state of the system
794 under analysis.
- 795 3. *Temporal and spatial resolutions and scales*: In this study, the spatial extent of the domains
796 was set to $1^{\circ} \times 1^{\circ}$ with an hourly temporal resolution over CONUS. Although these temporal
797 and spatial resolutions were appropriate to analyze mesoscale land-atmosphere circulations
798 with an ESM framework in mind, applications requiring finer or coarser temporal and spatial
799 resolutions (i.e., diurnal cycle evaluations) would most likely require the definition of a
800 different structure for the covariance function parametric model. It is possible that the
801 goodness of fit of analytical covariance functions may exhibit some dependence on the
802 domain size used in the analysis. Thus, further analysis of the proposed approach over
803 varying time windows, domain sizes, and spatio-temporal scales are also a welcome follow-
804 up contribution. Preliminary work by the coauthors has proved the utility of the ESTCF
805 approach in summarizing the spatio-temporal information contained within a long-term (i.e.,
806 > ten years of record length), global, remotely sensed LST gridded product (Freitas et al.,
807 2013). However, further analyses will examine the effects of the selected moving window

808 size, spatial offset, analyzed time period, and temporal aggregation in the obtained ESTCFs.
809 The accuracy of the proposed parametric covariance model under these varying conditions
810 will also be tested.

811 4.2.2 Remote sensing of LST and SST

812 In this study, a coupled LST-SST product was employed to explore the spatio-temporal
813 patterns of remote sensing surface temperature that could lead to the development of mesoscale
814 circulations. However, as mentioned in Section 2.1, remote sensing retrieval of LST and SST are
815 intrinsically different, with each of them presenting particular challenges.

816 Surface temperature remote sensing retrieval poses inherent challenges due to multiple
817 factors impacting measurement accuracy and precision. Among these challenges, the intrinsic
818 diversity of Earth's surface materials stands out. Each surface type possesses distinct thermal
819 characteristics, emissivity values, and heat exchange mechanisms, resulting in varying thermal
820 energy emission patterns. This diversity makes the algorithm heavily dependent on the feed
821 surface emissivity values and land-water mask. Furthermore, the presence of atmospheric water
822 vapor significantly affects the thermal infrared signal detected by satellites, often leading to an
823 underestimation of actual surface temperature compared to the measured brightness temperature.
824 The relationship between radiance and temperature is also nonlinear, rendering traditional linear
825 models, like the single and split channel methods, less precise, particularly in hot and humid
826 atmospheric conditions (Duffy et al., 2022). This discrepancy is amplified with increasing
827 column water vapor, making the inclusion of water vapor data crucial for enhancing LST
828 accuracy (Sobrino et al., 1993). However, the spatial and temporal variability of the atmospheric
829 conditions further complicates the retrieval process, as they introduce error propagation and
830 uncertainties into the estimates.

831 In this sense, remote sensing-derived surface states inevitably depend on assumptions
832 about the overlying atmosphere and landscape features, and estimations ultimately constitute a
833 model output. This produces a relatively high uncertainty, mainly since there is no observational
834 'truth' at the landscape scale for comparison (Stisen et al., 2011). However, the information
835 content present in the spatio-temporal structure of the observed satellite fields is intrinsically
836 valuable, especially when considering the wide variety of variables of surface states and fluxes
837 currently estimated (e.g., soil moisture content (Chan et al., 2018; Entekhabi et al., 2010; Kerr et
838 al., 2012; Parinussa et al., 2015; W. Wagner et al., 2013), evapotranspiration (Boschetti et al.,
839 2019; J. B. Fisher et al., 2020; Martens et al., 2017; Running et al., 2019; Su, 2002), snow cover
840 fraction (Painter et al., 2009; Tsai et al., 2019), and changes in water storage (Tapley et al.,
841 2004)).

842 4.3 ESTCF applications

843 4.3.1 Towards the improved representation of land-atmosphere interactions in ESMs

844 Research has established the significant role of landscape heterogeneities in key
845 atmospheric processes, including atmospheric boundary layer depth determination, convection
846 initiation, and mesoscale circulations (Bertoldi et al., 2013; Gutowski et al., 2020; Kang &
847 Bryan, 2011; Kustas & Albertson, 2003; Ntelekos et al., 2008; Simon et al., 2021; Timmermans
848 et al., 2010). Local studies are advancing our understanding of multi-scale landscape

849 heterogeneity effects on micro- and mesoscale meteorological processes (H. Y. Huang et al.,
850 2011; Senatore et al., 2015; Shrestha et al., 2014; Talbot et al., 2012). However, the extent of this
851 effect on land-atmosphere interactions in the broader climate system remains uncertain. This
852 uncertainty primarily stems from the limited coupling between existing sub-grid
853 parameterizations in land surface models and the atmospheric components of ESMs. Typically,
854 ESMs exchange spatial mean mass and energy fluxes between land and atmosphere while
855 disregarding higher-order spatial statistics, such as spatial variance or characteristic length
856 scales. Nevertheless, atmospheric circulation models are progressively incorporating higher-
857 order sub-grid scale processes, as seen in examples like the Cloud Layers Unified By Binormals
858 (CLUBB) and Eddy Diffusivity Mass Flux (EDMF) (Golaz et al., 2002; M. Huang et al., 2022;
859 Sušelj et al., 2013). These developments provide an opportunity for potential coupling between
860 atmospheric models and the sub-grid scale heterogeneity of the land surface. This study aims to
861 contribute meaningfully to such efforts, ideally enhancing land surface parameterizations within
862 the atmospheric components of ESMs with higher-order statistics.

863 The approach presented in this study can provide more than a tool to summarize the
864 spatio-temporal dependence structure of remotely sensed fields; it is proved that it can also be
865 employed to estimate the characteristic length scales of heterogeneity, providing
866 parametrizations with useful spatio-temporal information over macroscale grid cells. The method
867 also assesses the spatial coherence and memory of the fields and allows the identification of
868 regions with homogeneous characteristics. By identifying these locations, the tool could help
869 inform parametrizations schemes for ESMs by distinguishing locations and times for which the
870 common flux averaging methods might be insufficient to represent interactions between model
871 components, particularly the interaction between the land and atmosphere. Ultimately, the hope
872 is that the type of approach presented through this study drives the ESM community in a
873 direction where the representation of the subgrid-scale heterogeneity in both space and time is
874 considered both in model development and as a model diagnostic tool.

875 4.3.2 Model evaluation: Spatially distributed hydrological models and Land surface models

876 Physically based spatially distributed hydrological models allow the simulation of the
877 spatial distribution of hydrological and hydraulic processes within catchments while still
878 providing discharge estimates for the river network. Their main advantage is that they emulate,
879 to some extent, the natural spatial heterogeneity of the hydrological processes, driven by
880 spatially distributed factors that constrain the hydrological processes, such as land use, climate,
881 and soil properties (Koch et al., 2015). However, most spatially distributed hydrological models
882 are still calibrated and evaluated using a goodness of fit metric describing the efficiency of the
883 model representation of a catchment-aggregated or point-retrieved quantity, such as discharge
884 (Zink et al., 2018). This practice generally makes the models over-parametrized relative to the
885 data available to constrain them (Stisen et al., 2011). It is widely accepted that model calibration
886 and validation practices for these models should take directions that agree more with the spatially
887 distributed nature of the outputs, including continuous spatial observation data (Beven, 2001).
888 The main issue, however, is the lack of a standard set of techniques and metrics to evaluate the
889 goodness of fit of the models' spatial predictions. Several spatial performance metrics have been
890 developed (Ko et al., 2019; Koch et al., 2015, 2016, 2017; Li et al., 2009; Stisen et al., 2011,
891 2021; Xiao et al., 2022; Zink et al., 2018) and reviewed in their ability to constrain and evaluate
892 models (Wealands et al., 2005). In general, simple global statistics operating locally (i.e., pixel-
893 to-pixel comparison of the modeled and observed maps) are insufficient as they are susceptible

894 to small-scale spatial displacement errors and do not consider information on patterns or spatial
895 correlation of the data. More robust global statistical metrics such as mean bias, standard
896 deviation, and variogram ranges are not entirely appropriate, as they are also pattern agnostic. An
897 approach like the one presented in this study can provide a robust and compact tool to evaluate
898 the performance of spatially distributed hydrological models while still being “pattern aware”.
899 The model representation of spatio-temporal variables and processes such as soil moisture
900 content, runoff generation, infiltration, and evapotranspiration can be characterized using the
901 ESTCF tool; then, by adding catchment aggregated observations, such as streamflow, the
902 proposed tool would add an extra layer of constraints in the calibration stage. In addition to its
903 flexibility in terms of spatial and temporal resolution, the proposed ESTCF method has the
904 advantage of not being limited to square or rectangular domain shapes and being readily
905 applicable to catchment-based hydrological models.

906 On the other hand, land surface models (LSMs) were initially developed to operate at
907 continental and global scales as the land boundary condition of climate and numerical weather
908 prediction models and ESMs (R. A. Fisher & Koven, 2020; Ko et al., 2019). Recognizing the
909 multi-scale nature of spatial heterogeneity in land surface processes, tiling schemes were
910 developed to represent the hierarchical structure of heterogeneity within macroscale grid cells
911 (~100km horizontal resolution). Tiling schemes subdivide macroscale grid cells into smaller
912 units (i.e., tiles). Within this semi-distributed framework, each tile's water, energy, and carbon
913 cycles are resolved independently, assuming intra-tile homogeneity (D. Li et al., 2013). Despite
914 the significant advances regarding tiling schemes over the last decade, many issues persist,
915 including the fact that over large-scale domains, LSM sub-grid outputs are mostly only
916 summarized and evaluated via macroscale grid statistics: spatial mean and variance. Although
917 informative, these statistics are insensitive to the tiles' large-scale spatial patterns (i.e., pattern-
918 agnostic metrics) (Jupp & Twiss, 2006; Torres-Rojas et al., 2022). This issue is critical as
919 emerging work shows the importance of correctly representing the sub-grid spatio-temporal
920 patterns of surface states to explain the role of sub-grid heterogeneity on atmospheric response
921 (Simon et al., 2021). An approach as the ESTCF can provide a tool to summarize the spatio-
922 temporal dependence structure of LSM output fields, characterize it, and evaluate the accuracy of
923 the model parametrizations of different processes by comparison to remote sensing derived
924 ESTCF for multiple variables (e.g., soil moisture content, LST, evapotranspiration, and
925 vegetation condition indexes, among others).

926 Nevertheless, when assessing either distributed hydrological models or LSMs in relation
927 to hydrological states or fluxes derived from remote sensing, one must acknowledge that this
928 involves comparing models to models, with considerable uncertainty inherent in both methods.
929 This is especially true as there is no definitive observational ‘truth’ available for landscape-scale
930 comparisons. Furthermore, the careful selection of suitable evaluation variables and objective
931 functions is essential to guarantee the reliability of model assessments (Stisen et al., 2011).

932 4.3.3 Spatio-temporal characterization for alternative applications

933 This study introduces the ESTCF as a versatile and comprehensive tool to depict and
934 characterize the spatio-temporal interdependence structure of remotely sensed fields. Even
935 though the tool is solely applied to LST fields in this study, it is recognized that application to
936 other spatio-temporal fields might shed light on the dynamics of processes within different
937 compartments of the SVAS. This section explores both the remote sensing data available for

938 other applications and systems and the processes that would benefit from the application of the
939 ESTCF method.

- 940 ▪ Soil moisture content (SMC): Besides the relevance of soil moisture spatio-temporal
941 patterns in the initiation of land-atmosphere circulations (see Section 1), other essential
942 processes such as drought onset and evolution, infiltration, surface and subsurface runoff,
943 and inundation dynamics, all heavily depend on the spatio-temporal structure of SMC
944 fields. However, the main limitations of the currently available SMC remote sensing
945 products are their long revisit times and low spatial resolution. These limiting factors
946 reduce the current applicability of the proposed methods to all the mentioned processes.
947 However, regional flood and drought evolution analyses on longer time scales (biweekly
948 to monthly) are still feasible using the available data.
- 949 ▪ Fractional vegetation cover (FVC), leaf area index (LAI), normalized difference
950 vegetation index (NDVI), and enhanced vegetation index (EVI): Spatio-temporal
951 remotely sensed fields of vegetation-related quantities and indices contain essential
952 information related to processes such as evapotranspiration, erosion, net primary
953 productivity, crop productivity, agricultural droughts, and turbulent energy exchange
954 between the land surface and the atmosphere. The temporal and spatial resolution of the
955 currently available products would enable weekly to monthly analysis over seasonal
956 scales and regional to continental domains.
- 957 ▪ Evapotranspiration (ET): ET is a critical process in the hydrological cycle, linking the
958 land surface water balance, carbon cycle, and the land surface energy balance. Remote
959 sensing provides a method to estimate ET at regional to global scales with biweekly to
960 weekly return rates. Spatio-temporal analysis of this variable would be primarily valuable
961 for model evaluation and calibration purposes due to the vital role of estimated ET in
962 model structures.
- 963 ▪ Reanalysis of atmospheric, land, and oceanic climate variables: Global, hourly, and
964 extended records (~1940-present) of multiple variables related to different compartments
965 of the SVAS are included within reanalysis datasets. The wide availability of this data
966 might allow us to analyze the impacts of climate variability and climate change on the
967 spatio-temporal dependence structure of multiple fluxes and states in systems within the
968 SVAS.

969 **5 Summary and Conclusions**

970 Several approaches have been developed to identify, summarize, and extract relevant
971 patterns from spatio-temporal geophysical datasets. These methods can be applied in both space
972 and time, though, in general, they are only meant to analyze independent dimensions. In climate,
973 environmental, and hydrological applications, there is a clear advantage in concurrently detecting
974 spatially connected and enduring structures or patterns as they offer insights into the dynamics of
975 the processes influencing them. Among the tools developed for geostatistical analysis, the
976 ESTCF stands out for its simplicity. Under several assumptions, the ESTCF quantifies the
977 strength and structure of dependence between different locations and times. Once the ESTCF is
978 computed, it becomes possible to select a parametric covariance model and estimate its
979 parameters by fitting the model to the empirical function. This process allows us to gain insights
980 into the spatio-temporal properties and interactions of the original field based on the estimated
981 parameters.

982 This study introduced the ESTCF as a tool for evaluating the spatial consistency and
983 temporal persistence of remotely sensed spatio-temporal fields. It was used to identify patterns
984 that could have significance in understanding the dynamics of processes within the Soil-
985 Vegetation-Atmosphere System (SVAS). Additionally, the study presented a parametric
986 covariance model to summarize the spatio-temporal structure revealed by the ESTCF. These
987 tools were then applied to remotely sensed LST fields over CONUS. The objective was to
988 determine whether applying these tools could help pinpoint areas where landscape features
989 played a role in initiating land-atmosphere circulation systems. Furthermore, the study proposed
990 a metric for assessing the combined spatio-temporal persistence of the analyzed fields and a
991 clustering approach to identify areas with homogeneous spatio-temporal dependence structures.
992 Thus, the critical developments in this study included (a) a flexible and comprehensive tool to
993 characterize and represent the spatio-temporal dependence structure of remotely sensed fields in
994 the form of the ESTCF, (b) a 4-parameter covariance function model to more concisely describe
995 the spatio-temporal patterns captured with the ESTCF, and (c) a multi-dimensional clustering
996 approach to determine areas with similar spatio-temporal dependence structures, and consequently a
997 consistent presumed land-atmosphere circulation potential.

998 The ESTCF, derived from remotely sensed observations, was readily accessible and
999 demonstrated adaptability in handling missing data, varying domain sizes, and different temporal
1000 aggregations. It showcased its capacity to characterize spatio-temporal patterns using field
1001 characteristics like spatio-temporal variance, spatial coherence structure, temporal persistence,
1002 and space-time interactions. The proposed parametric covariance function model was also
1003 reasonably accurate in emulating the empirical data while succinctly summarizing its dynamics.
1004 The simplified attributes were then utilized to pinpoint regions with consistent spatio-temporal
1005 patterns, effectively categorizing domains based on their primary spatio-temporal characteristics.
1006 The combined use of the clustering procedure and the suggested combined metric for spatio-
1007 temporal persistence facilitated the identification of zones with increased spatio-temporal
1008 dynamics. These zones included coastal areas in the Gulf of California and the South Pacific
1009 region, and regions with high elevations, such as the Sierra Nevada, Rockies, Coastal Ranges,
1010 and Appalachian Mountains. Additionally, the method identified coastal regions surrounding the
1011 largest lakes in the Great Lakes area. These findings aligned with prior literature reports
1012 suggesting an increased likelihood of mesoscale land-atmosphere circulations in locations with
1013 those landscape features. These results, however, were specific to the selected domain size,
1014 temporal aggregation, and parametric model structure. As such, it is recognized that this is just
1015 one of the many possibilities to summarize the spatio-temporal dynamics from remotely sensed
1016 fields and that more efficient and accurate strategies might exist.

1017 The developed approach is the first attempt to objectively analyze the complex spatio-
1018 temporal dependence structure from remotely sensed fields for analysis applications. Moving
1019 forward, the transferability of the approach should be tested under various data availability
1020 scenarios, parametric model functional forms, clustering techniques, temporal windows, domain
1021 sizes, and study areas (i.e., move to global scales). Furthermore, although subject to errors and
1022 biases, using LST remotely sensed fields might help inform land-atmosphere parametrization
1023 schemes for ESMs of the real spatio-temporal distribution of the surface fluxes. The introduced
1024 approach will also be beneficial in calibrating and evaluating process-based spatially distributed
1025 hydrological models and parametrizations for LSMs. The approach can also be easily transferred
1026 to several other available remote sensing data sources, enhancing our understanding of the
1027 spatio-temporal dynamics of processes within different compartments of the SVAS. This work

1028 represents a step toward adapting model evaluation and parametrization techniques to leverage
1029 the available high-resolution data better, accounting for the dynamic nature of land surface
1030 processes. Overall, the tools introduced here provide a path forward to formally identify and
1031 summarize the spatio-temporal patterns observed in remotely sensed fields and relate those to the
1032 footprint of more complex dynamic processes within the SVAS.

1033

1034 **Acknowledgments**

1035 This study was supported by funding from NOAA grants NA19OAR4310241 (Parameterizing
1036 the effects of sub-grid land heterogeneity on the atmospheric boundary layer and convection:
1037 Implications for surface climate, variability, and extremes) and NA22OAR4310644
1038 (Implications of heterogeneity-aware land-atmosphere coupling in the predictability of
1039 precipitation extremes).

1040 **Open Research**

1041 The GOES-16 LST and SST products used in this study are freely available from NOAA's
1042 Comprehensive Large Array-Data Stewardship System (CLASS). The data that support the findings
1043 of this study, including the scripts to reproject the original data to a WSG84 projection, combine LST
1044 and SST products for the CONUS region, merge individual hourly files into weekly netCDF4 files,
1045 extract the data for 1°x1° domains over CONUS, compute the daytime summer ESTCF for those
1046 domains, and analyze the results (i.e., mapping and clustering) are preserved at
1047 <https://doi.org/10.5281/zenodo.8428629> (Torres-Rojas & Chaney, 2023).

1048 **References**

- 1049 Anderson, M. C., Kustas, W. P., Alfieri, J. G., Gao, F., Hain, C., Prueger, J. H., et al. (2012).
1050 Mapping daily evapotranspiration at Landsat spatial scales during the BEAREX '08 field
1051 campaign. *Advances in Water Resources*, 50, 162–177.
1052 <https://doi.org/http://dx.doi.org/10.1016/j.advwatres.2012.06.005>
- 1053 Bertoldi, G., Kustas, W. P., & Albertson, J. D. (2013). Evaluating Source Area Contributions
1054 from Aircraft Flux Measurements Over Heterogeneous Land Using Large-Eddy Simulation.
1055 *Boundary-Layer Meteorology*, 147(2), 261–279. <https://doi.org/10.1007/s10546-012-9781-y>
- 1056 Beven, K. (2001). How far can we go in distributed hydrological modelling? *Hydrology and*
1057 *Earth System Sciences*, 5(1), 1–12. <https://doi.org/10.5194/hess-5-1-2001>

- 1058 Biswas, A. (2014). Scaling analysis of soil water storage with missing measurements using the
1059 second-generation continuous wavelet transform. *European Journal of Soil Science*, 65(4),
1060 594–604. <https://doi.org/10.1111/ejss.12145>
- 1061 Bolliger, J., Wagner, H. H., & Turner, M. G. (2007). Identifying and Quantifying Landscape
1062 Patterns in Space and Time, 177–194. https://doi.org/10.1007/978-1-4020-4436-6_12
- 1063 Boschetti, L., Roy, D. P., Giglio, L., Huang, H., Zubkova, M., & Humber, M. L. (2019). Global
1064 validation of the collection 6 MODIS burned area product. *Remote Sensing of Environment*,
1065 235, 111490. <https://doi.org/10.1016/J.RSE.2019.111490>
- 1066 Brunsell, N., & Gillies, R. R. (2003). Scale issues in land - Atmosphere interactions:
1067 Implications for remote sensing of the surface energy balance. *Agricultural and Forest*
1068 *Meteorology*, 117(3–4), 203–221. [https://doi.org/10.1016/S0168-1923\(03\)00064-9](https://doi.org/10.1016/S0168-1923(03)00064-9)
- 1069 Chan, S. K., Bindlish, R., O’Neill, P., Jackson, T., Njoku, E., Dunbar, S., et al. (2018).
1070 Development and assessment of the SMAP enhanced passive soil moisture product. *Remote*
1071 *Sensing of Environment*, 204, 931–941. <https://doi.org/10.1016/J.RSE.2017.08.025>
- 1072 Chaney, N. W., Wood, E. F., Mcbratney, A. B., Hempel, J. W., Nauman, T. W., Brungard, C.
1073 W., & Odgers, N. P. (2016). POLARIS: A 30-meter probabilistic soil series map of the
1074 contiguous United States POLARIS: A 30-meter probabilistic soil series map of the
1075 contiguous United States. *Geoderma*, 274, 54–67.
1076 <https://doi.org/10.1016/j.geoderma.2016.03.025>
- 1077 Chang, Y., Xiao, J., Li, X., Froking, S., Zhou, D., Schneider, A., et al. (2021). Exploring diurnal
1078 cycles of surface urban heat island intensity in Boston with land surface temperature data
1079 derived from GOES-R geostationary satellites. *Science of the Total Environment*, 763,
1080 144224. <https://doi.org/10.1016/j.scitotenv.2020.144224>
- 1081 Chen, F., & Avissar, R. (1994). The Impact of Land-Surface Wetness Heterogeneity on
1082 Mesoscale Heat Fluxes. *Journal of Applied Meteorology*, 33(11), 1323–1340.
1083 [https://doi.org/10.1175/1520-0450\(1994\)033<1323:tiolsw>2.0.co;2](https://doi.org/10.1175/1520-0450(1994)033<1323:tiolsw>2.0.co;2)
- 1084 Chen, W., Genton, M. G., & Sun, Y. (2021). Space-time covariance structures and models.
1085 *Annual Review of Statistics and Its Application*, 8, 191–215.
1086 <https://doi.org/10.1146/annurev-statistics-042720-115603>
- 1087 Cheng, W. Y. Y., & Cotton, W. R. (2004). Sensitivity of a cloud-resolving simulation of the
1088 genesis of a mesoscale convective system to horizontal heterogeneities in soil moisture
1089 initialization. *Journal of Hydrometeorology*, 5(5), 934–958. [https://doi.org/10.1175/1525-7541\(2004\)005<0934:SOACSO>2.0.CO;2](https://doi.org/10.1175/1525-7541(2004)005<0934:SOACSO>2.0.CO;2)
- 1091 Courault, D., Drobinski, P., Brunet, Y., Lacarrere, P., & Talbot, C. (2007). Impact of surface
1092 heterogeneity on a buoyancy-driven convective boundary layer in light winds. *Boundary-*
1093 *Layer Meteorology*, 124(3), 383–403. <https://doi.org/10.1007/s10546-007-9172-y>
- 1094 Cressie, N., & Huang, H. C. (1999). Classes of Nonseparable, Spatio-Temporal Stationary
1095 Covariance Functions. *Journal of the American Statistical Association*, 94(448), 1330–
1096 1339. <https://doi.org/10.1080/01621459.1999.10473885>
- 1097 Cressie, N., & Wikle, C. (2015). *Statistics for Spatio-Temporal Data*. Hoboken, New Jersey:
1098 John Wiley & Sons, Ltd.

- 1099 Crow, W. T., Huffman, G. J., Bindlish, R., & Jackson, T. J. (2009). Improving satellite-based
1100 rainfall accumulation estimates using spaceborne surface soil moisture retrievals. *Journal of*
1101 *Hydrometeorology*, *10*(1), 199–212. <https://doi.org/10.1175/2008JHM986.1>
- 1102 Demel, S. S., & Du, J. (2015). Spatio-temporal models for some data sets in continuous space
1103 and discrete time. *Statistica Sinica*, *25*(1), 81–98. <https://doi.org/10.5705/ss.2013.223w>
- 1104 Desai, A. R., Khan, A. M., Zheng, T., Paleri, S., Butterworth, B., Lee, T. R., et al. (2021). Multi-
1105 Sensor Approach for High Space and Time Resolution Land Surface Temperature. *Earth*
1106 *and Space Science*, *8*(10), 1–18. <https://doi.org/10.1029/2021EA001842>
- 1107 Devadoss, J., Falco, N., Dafflon, B., Wu, Y., Franklin, M., Hermes, A., et al. (2020). Remote
1108 sensing-informed zonation for understanding snow, plant and soil moisture dynamics within
1109 a mountain ecosystem. *Remote Sensing*, *12*(17), 2733. <https://doi.org/10.3390/RS12172733>
- 1110 Dickinson, R. E. (1995). Land-atmosphere interaction. *Reviews of Geophysics*, *33*(2 S), 917–922.
1111 <https://doi.org/10.1029/95RG00284>
- 1112 Dirmeyer, P. A., Jin, Y., Singh, B., & Yan, X. (2013). Trends in land-atmosphere interactions
1113 from CMIP5 simulations. *Journal of Hydrometeorology*, *14*(3), 829–849.
1114 <https://doi.org/10.1175/JHM-D-12-0107.1>
- 1115 Duffy, K., Vandal, T. J., & Nemani, R. R. (2022). Multisensor Machine Learning to Retrieve
1116 High Spatiotemporal Resolution Land Surface Temperature. *IEEE Access*, *10*(August),
1117 89221–89231. <https://doi.org/10.1109/ACCESS.2022.3198673>
- 1118 Entekhabi, D., Njoku, E. G., O’Neill, P. E., Kellogg, K. H., Crow, W. T., Edelstein, W. N., et al.
1119 (2010). The soil moisture active passive (SMAP) mission. *Proceedings of the IEEE*, *98*(5),
1120 704–716. <https://doi.org/10.1109/JPROC.2010.2043918>
- 1121 Faghmous, J. H., & Kumar, V. (2014). Spatio-temporal Data Mining for Climate Data:
1122 Advances, Challenges, and Opportunities (pp. 83–116). [https://doi.org/10.1007/978-3-642-](https://doi.org/10.1007/978-3-642-40837-3_3)
1123 [40837-3_3](https://doi.org/10.1007/978-3-642-40837-3_3)
- 1124 Fang, L., Yu, Y., Xu, H., & Sun, D. (2014). New retrieval algorithm for deriving land surface
1125 temperature from geostationary orbiting satellite observations. *IEEE Transactions on*
1126 *Geoscience and Remote Sensing*, *52*(2), 819–828.
1127 <https://doi.org/10.1109/TGRS.2013.2244213>
- 1128 Fang, Z., Bogena, H., Kollet, S., Koch, J., & Vereecken, H. (2015). Spatio-temporal validation of
1129 long-term 3D hydrological simulations of a forested catchment using empirical orthogonal
1130 functions and wavelet coherence analysis. *Journal of Hydrology*, *529*, 1754–1767.
1131 <https://doi.org/10.1016/J.JHYDROL.2015.08.011>
- 1132 Ferguson, C. R., & Wood, E. F. (2011). Observed land-atmosphere coupling from satellite
1133 remote sensing and reanalysis. *Journal of Hydrometeorology*, *12*(6), 1221–1254.
1134 <https://doi.org/10.1175/2011JHM1380.1>
- 1135 Ferguson, C. R., Wood, E. F., & Vinukollu, R. K. (2012). A Global intercomparison of modeled
1136 and observed land-atmosphere coupling. *Journal of Hydrometeorology*, *13*(3), 749–784.
1137 <https://doi.org/10.1175/JHM-D-11-0119.1>
- 1138 Fisher, J. B., Lee, B., Purdy, A. J., Halverson, G. H., Dohlen, M. B., Cawse-Nicholson, K., et al.
1139 (2020). ECOSTRESS: NASA’s Next Generation Mission to Measure Evapotranspiration

- 1140 From the International Space Station. *Water Resources Research*, 56(4), e2019WR026058.
1141 <https://doi.org/10.1029/2019WR026058>
- 1142 Fisher, R. A., & Koven, C. D. (2020, April 1). Perspectives on the Future of Land Surface
1143 Models and the Challenges of Representing Complex Terrestrial Systems. *Journal of*
1144 *Advances in Modeling Earth Systems*. Blackwell Publishing Ltd.
1145 <https://doi.org/10.1029/2018MS001453>
- 1146 Freitas, S. C., Trigo, I. F., Macedo, J., Barroso, C., Silva, R., & Perdigão, R. (2013). Land
1147 surface temperature from multiple geostationary satellites. *International Journal of Remote*
1148 *Sensing*, 34(9–10), 3051–3068. <https://doi.org/10.1080/01431161.2012.716925>
- 1149 Gentine, P., Massmann, A., Lintner, B. R., Hamed Alemohammad, S., Fu, R., Green, J. K., et al.
1150 (2019). Land-atmosphere interactions in the tropics - A review. *Hydrology and Earth*
1151 *System Sciences*, 23(10), 4171–4197. <https://doi.org/10.5194/hess-23-4171-2019>
- 1152 Gneiting, T. (2002). Nonseparable, stationary covariance functions for space-time data. *Journal*
1153 *of the American Statistical Association*, 97(458), 590–600.
1154 <https://doi.org/10.1198/016214502760047113>
- 1155 Golaz, J. C., Larson, V. E., & Cotton, W. R. (2002). A PDF-based model for boundary layer
1156 clouds. Part I: Method and model description. *Journal of the Atmospheric Sciences*, 59(24),
1157 3540–3551. [https://doi.org/10.1175/1520-0469\(2002\)059<3540:APBMFB>2.0.CO;2](https://doi.org/10.1175/1520-0469(2002)059<3540:APBMFB>2.0.CO;2)
- 1158 Graf, A., Herbst, M., Weihermüller, L., Huisman, J. A., Prolingheuer, N., Bornemann, L., &
1159 Vereecken, H. (2012). Analyzing spatiotemporal variability of heterotrophic soil respiration
1160 at the field scale using orthogonal functions. *Geoderma*, 181–182, 91–101.
1161 <https://doi.org/10.1016/j.geoderma.2012.02.016>
- 1162 Gueting, N., Klotzsche, A., van der Kruk, J., Vanderborght, J., Vereecken, H., & Englert, A.
1163 (2015). Imaging and characterization of facies heterogeneity in an alluvial aquifer using
1164 GPR full-waveform inversion and cone penetration tests. *Journal of Hydrology*, 524, 680–
1165 695. <https://doi.org/10.1016/j.jhydrol.2015.03.030>
- 1166 Gutowski, W. J., Ullrich, P. A., Hall, A., Leung, L. R., O'Brien, T. A., Patricola, C. M., et al.
1167 (2020). The Ongoing Need for High-Resolution Regional Climate Models: Process
1168 Understanding and Stakeholder Information. *Bulletin of the American Meteorological*
1169 *Society*, 101(5), E664–E683. <https://doi.org/10.1175/BAMS-D-19-0113.1>
- 1170 Guttorp, P., & Sampson, P. D. (1994). 20 Methods for estimating heterogeneous spatial
1171 covariance functions with environmental applications. *Handbook of Statistics*, 12, 661–689.
1172 [https://doi.org/10.1016/S0169-7161\(05\)80022-7](https://doi.org/10.1016/S0169-7161(05)80022-7)
- 1173 Haas, T. C. (1990a). Kriging and automated variogram modeling within a moving window.
1174 *Atmospheric Environment Part A, General Topics*, 24(7), 1759–1769.
1175 [https://doi.org/10.1016/0960-1686\(90\)90508-K](https://doi.org/10.1016/0960-1686(90)90508-K)
- 1176 Haas, T. C. (1990b). Lognormal and moving window methods of estimating acid deposition.
1177 *Journal of the American Statistical Association*, 85(412), 950–963.
1178 <https://doi.org/10.1080/01621459.1990.10474966>
- 1179 Hashimoto, H., Wang, W., Dungan, J. L., Li, S., Michaelis, A. R., Takenaka, H., et al. (2021).
1180 New generation geostationary satellite observations support seasonality in greenness of the

- 1181 Amazon evergreen forests. *Nature Communications*, 12(1). [https://doi.org/10.1038/s41467-](https://doi.org/10.1038/s41467-021-20994-y)
1182 021-20994-y
- 1183 Holzman, M. E., Rivas, R., & Bayala, M. (2014). Subsurface soil moisture estimation by VI-LST
1184 method. *IEEE Geoscience and Remote Sensing Letters*, 11(11), 1951–1955.
1185 <https://doi.org/10.1109/LGRS.2014.2314617>
- 1186 Hook, S., & Hulley, G. (2019). ECOSTRESS Land Surface Temperature and Emissivity Daily
1187 L2 Global 70 m V001.
1188 <https://doi.org/https://doi.org/10.5067/ECOSTRESS/ECO2LSTE.001>
- 1189 Huang, H. Y., Margulis, S. A., Chu, C. R., & Tsai, H. C. (2011). Investigation of the impacts of
1190 vegetation distribution and evaporative cooling on synthetic urban daytime climate using a
1191 coupled LES-LSM model. *Hydrological Processes*, 25(10), 1574–1586.
1192 <https://doi.org/10.1002/hyp.7919>
- 1193 Huang, M., Ma, P. L., Chaney, N. W., Hao, D., Bisht, G., Fowler, M. D., et al. (2022).
1194 Representing surface heterogeneity in land–atmosphere coupling in E3SMv1 single-column
1195 model over ARM SGP during summertime. *Geoscientific Model Development*, 15(16),
1196 6371–6384. <https://doi.org/10.5194/gmd-15-6371-2022>
- 1197 de Iaco, S. (2010). Space-time correlation analysis: A comparative study. *Journal of Applied*
1198 *Statistics*, 37(6), 1027–1041. <https://doi.org/10.1080/02664760903019422>
- 1199 Ignatov, A., Pennybacker, M., Gladkova, I., Petrenko, B., Jonasson, O., & Kihai, Y. (2019).
1200 GHRSSST NOAA/STAR GOES-16 ABI L2P America Region SST v2.70 dataset (GDS
1201 version 2). <https://doi.org/https://doi.org/10.25921/ayf6-c438>
- 1202 Jenny, H. (1941). *Factors of Soil Formation, a System of Quantitative Pedology*. New York, NY:
1203 McGraw-Hill. <https://doi.org/10.2134/agronj1941.00021962003300090016x>
- 1204 Jung, M., Reichstein, M., Margolis, H. A., Cescatti, A., Richardson, A. D., Arain, M. A., et al.
1205 (2011). Global patterns of land-atmosphere fluxes of carbon dioxide, latent heat, and
1206 sensible heat derived from eddy covariance, satellite, and meteorological observations.
1207 *Journal of Geophysical Research: Biogeosciences*, 116(3), 1–16.
1208 <https://doi.org/10.1029/2010JG001566>
- 1209 Jupp, T. E., & Twiss, S. D. (2006). A physically motivated index of subgrid-scale pattern.
1210 *Journal of Geophysical Research Atmospheres*, 111(19), 19112.
1211 <https://doi.org/10.1029/2006JD007343>
- 1212 Kang, S. L., & Bryan, G. H. (2011). A Large-Eddy Simulation Study of Moist Convection
1213 Initiation over Heterogeneous Surface Fluxes. *Monthly Weather Review*, 139(9), 2901–
1214 2917. <https://doi.org/10.1175/MWR-D-10-05037.1>
- 1215 Katul, G., & Parlange, M. B. (1995). Analysis of Land Surface Heat Fluxes Using the
1216 Orthonormal Wavelet Approach. *Water Resources Research*, 31(11), 2743–2749.
1217 <https://doi.org/10.1029/95WR00003>
- 1218 Katul, G., Lai, C. T., Schäfer, K., Vidakovic, B., Albertson, J., Ellsworth, D., & Oren, R. (2001).
1219 Multiscale analysis of vegetation surface fluxes: From seconds to years. *Advances in Water*
1220 *Resources*, 24(9–10), 1119–1132. [https://doi.org/10.1016/S0309-1708\(01\)00029-X](https://doi.org/10.1016/S0309-1708(01)00029-X)
- 1221 Kerr, Y., Waldteufel, P., Richaume, P., Wigneron, J. P., Ferrazzoli, P., Mahmoodi, A., et al.

- 1222 (2012). The SMOS soil moisture retrieval algorithm. *IEEE Transactions on Geoscience and*
1223 *Remote Sensing*, 50(5 PART 1), 1384–1403. <https://doi.org/10.1109/TGRS.2012.2184548>
- 1224 Kim, G., & Barros, A. P. (2002). Space-time characterization of soil moisture from passive
1225 microwave remotely sensed imagery and ancillary data. *Remote Sensing of Environment*,
1226 81(2–3), 393–403. [https://doi.org/10.1016/S0034-4257\(02\)00014-7](https://doi.org/10.1016/S0034-4257(02)00014-7)
- 1227 Ko, A., Mascaro, G., & Vivoni, E. R. (2019). Strategies to Improve and Evaluate Physics-Based
1228 Hyperresolution Hydrologic Simulations at Regional Basin Scales. *Water Resources*
1229 *Research*, (iii), 1129–1152. <https://doi.org/10.1029/2018WR023521>
- 1230 Koch, J., Jensen, K. H., & Stisen, S. (2015). Toward a true spatial model evaluation in
1231 distributed hydrological modeling: Kappa statistics, Fuzzy theory, and EOF-analysis
1232 benchmarked by the human perception and evaluated against a modeling case study. *Water*
1233 *Resources Research*, 51(2), 1225–1246. <https://doi.org/10.1002/2014WR016607>
- 1234 Koch, J., Siemann, A., Stisen, S., & Sheffield, J. (2016). Spatial validation of large-scale land
1235 surface models against monthly land surface temperature patterns using innovative
1236 performance metrics. *Journal of Geophysical Research*, 121(10), 5430–5452.
1237 <https://doi.org/10.1002/2015JD024482>
- 1238 Koch, J., Mendiguren, G., Mariethoz, G., & Stisen, S. (2017). Spatial sensitivity analysis of
1239 simulated land surface patterns in a catchment model using a set of innovative spatial
1240 performance metrics. *Journal of Hydrometeorology*, 18(4), 1121–1142.
1241 <https://doi.org/10.1175/JHM-D-16-0148.1>
- 1242 Korres, W., Koyama, C. N., Fiener, P., & Schneider, K. (2010). Analysis of surface soil moisture
1243 patterns in agricultural landscapes using Empirical Orthogonal Functions. *Hydrology and*
1244 *Earth System Sciences*, 14(5), 751–764. <https://doi.org/10.5194/hess-14-751-2010>
- 1245 Kustas, W. P., & Albertson, J. D. (2003). Effects of surface temperature contrast on land-
1246 atmosphere exchange: A case study from Monsoon 90. *Water Resources Research*, 39(6),
1247 1159. <https://doi.org/10.1029/2001WR001226>
- 1248 Laherrère, J., & Sornette, D. (1998). Stretched exponential distributions in nature and economy:
1249 “fat tails” with characteristic scales. *Eur. Phys. J. B*, 2, 525–539. Retrieved
1250 from <https://link.springer.com/content/pdf/10.1007/s100510050276.pdf>
- 1251 Lee, S. J., Wentz, E. A., & Gober, P. (2010). Space-time forecasting using soft geostatistics: A
1252 case study in forecasting municipal water demand for Phoenix, Arizona. *Stochastic*
1253 *Environmental Research and Risk Assessment*, 24(2), 283–295.
1254 <https://doi.org/10.1007/s00477-009-0317-z>
- 1255 Levine, P. A., Randerson, J. T., Swenson, S. C., & Lawrence, D. M. (2016). Evaluating the
1256 strength of the land-atmosphere moisture feedback in Earth system models using satellite
1257 observations. *Hydrology and Earth System Sciences*, 20(12), 4837–4856.
1258 <https://doi.org/10.5194/hess-20-4837-2016>
- 1259 Li, D., Bou-Zeid, E., Barlage, M., Chen, F., & Smith, J. A. (2013). Development and evaluation
1260 of a mosaic approach in the WRF-Noah framework. *Journal of Geophysical Research:*
1261 *Atmospheres*, 118(21), 11,918–11,935. <https://doi.org/10.1002/2013JD020657>
- 1262 Li, H. T., Brunner, P., Kinzelbach, W., Li, W. P., & Dong, X. G. (2009). Calibration of a

- 1263 groundwater model using pattern information from remote sensing data. *Journal of*
1264 *Hydrology*, 377(1–2), 120–130. <https://doi.org/10.1016/j.jhydrol.2009.08.012>
- 1265 Li, K., Guan, K., Jiang, C., Wang, S., Peng, B., & Cai, Y. (2021). Evaluation of Four New Land
1266 Surface Temperature (LST) Products in the U.S. Corn Belt: ECOSTRESS, GOES-R,
1267 Landsat, and Sentinel-3. *IEEE Journal of Selected Topics in Applied Earth Observations*
1268 *and Remote Sensing*, 14, 9931–9945. <https://doi.org/10.1109/JSTARS.2021.3114613>
- 1269 Ma, C. (2003). Spatio-temporal stationary covariance models. *Journal of Multivariate Analysis*,
1270 86(1), 97–107. [https://doi.org/10.1016/S0047-259X\(02\)00014-3](https://doi.org/10.1016/S0047-259X(02)00014-3)
- 1271 Mahfouf, J.-F., Richard, E., & Mascart, P. (1987). The Influence of Soil and Vegetation on the
1272 Development of Mesoscale Circulations. *Journal of Climate and Applied Meteorology*,
1273 26(11), 1483–1495. [https://doi.org/10.1175/1520-0450\(1987\)026<1483:TIOSAV>2.0.CO;2](https://doi.org/10.1175/1520-0450(1987)026<1483:TIOSAV>2.0.CO;2)
- 1274 Mälicke, M., Hassler, S. K., Blume, T., Weiler, M., & Zehe, E. (2020). Soil moisture: variable in
1275 space but redundant in time. *Hydrol. Earth Syst. Sci*, 24, 2633–2653.
1276 <https://doi.org/10.5194/hess-24-2633-2020>
- 1277 Martens, B., Miralles, D. G., Lievens, H., Van Der Schalie, R., De Jeu, R. A. M., Fernández-
1278 Prieto, D., et al. (2017). GLEAM v3: Satellite-based land evaporation and root-zone soil
1279 moisture. *Geoscientific Model Development*, 10(5), 1903–1925.
1280 <https://doi.org/10.5194/gmd-10-1903-2017>
- 1281 Martini, E., Wollschläger, U., Kögler, S., Behrens, T., Dietrich, P., Reinstorf, F., et al. (2015).
1282 Spatial and Temporal Dynamics of Hillslope-Scale Soil Moisture Patterns: Characteristic
1283 States and Transition Mechanisms. *Vadose Zone Journal*, 14(4), 1–16.
1284 <https://doi.org/10.2136/VZJ2014.10.0150>
- 1285 Matheron, G. (1989). Estimating and Choosing. *Estimating and Choosing*.
1286 <https://doi.org/10.1007/978-3-642-48817-7>
- 1287 Montero, J.-M., Fernández-Avilés, G., & Mateu, J. (2015). *Spatial and Spatio-Temporal*
1288 *Geostatistical Modeling and Kriging* (1st ed.). New York, NY: Wiley.
- 1289 Nair, U. S., Wu, Y., Kala, J., Lyons, T. J., Pielke, R. A., & Hacker, J. M. (2011). The role of land
1290 use change on the development and evolution of the west coast trough, convective clouds,
1291 and precipitation in southwest Australia. *Journal of Geophysical Research Atmospheres*,
1292 116(7), 1–12. <https://doi.org/10.1029/2010JD014950>
- 1293 Nicholson, S. E. (1988). Land surface atmosphere interaction: Physical processes and surface
1294 changes and their impact. *Progress in Physical Geography*, 12(1), 36–65.
1295 <https://doi.org/10.1177/030913338801200102>
- 1296 Ntelekos, A. A., Smith, J. A., Baeck, M. L., Krajewski, W. F., Miller, A. J., & Goska, R. (2008).
1297 Extreme hydrometeorological events and the urban environment: Dissecting the 7 July 2004
1298 thunderstorm over the Baltimore MD Metropolitan Region. *Water Resources Research*,
1299 44(8), 8446. <https://doi.org/10.1029/2007WR006346>
- 1300 Painter, T. H., Rittger, K., McKenzie, C., Slaughter, P., Davis, R. E., & Dozier, J. (2009).
1301 Retrieval of subpixel snow covered area, grain size, and albedo from MODIS. *Remote*
1302 *Sensing of Environment*, 113(4), 868–879. <https://doi.org/10.1016/J.RSE.2009.01.001>
- 1303 Paleri, S., Butterworth, B., & Desai, A. R. (2022). *Here, there, and everywhere: Spatial patterns*

- 1304 *and scales. Conceptual Boundary Layer Meteorology: The Air Near Here.* Elsevier Inc.
1305 <https://doi.org/10.1016/B978-0-12-817092-2.00009-6>
- 1306 Parinussa, R. M., Holmes, T. R. H., Wanders, N., Dorigo, W. A., & De Jeu, R. A. M. (2015). A
1307 Preliminary Study toward Consistent Soil Moisture from AMSR2. *Journal of*
1308 *Hydrometeorology*, *16*(2), 932–947. <https://doi.org/10.1175/JHM-D-13-0200.1>
- 1309 Petrenko, B., Ignatov, A., Kihai, Y., & Heidinger, A. (2010). Clear-sky mask for the advanced
1310 clear-sky processor for oceans. *Journal of Atmospheric and Oceanic Technology*, *27*(10),
1311 1609–1623. <https://doi.org/10.1175/2010JTECHA1413.1>
- 1312 Petrenko, B., Ignatov, A., Kihai, Y., Stroup, J., & Dash, P. (2014). Evaluation and selection of
1313 SST regression algorithms for JPSS VIIRS. *Journal of Geophysical Research:*
1314 *Atmospheres*, *119*(8), 4580–4599. <https://doi.org/10.1002/2013JD020637>
- 1315 Phillips, T. J., Klein, S. A., Ma, H. Y., Tang, Q., Xie, S., Williams, I. N., et al. (2017). Using
1316 ARM Observations to Evaluate Climate Model Simulations of Land-Atmosphere Coupling
1317 on the U.S. Southern Great Plains. *Journal of Geophysical Research: Atmospheres*,
1318 *122*(21), 11,524–11,548. <https://doi.org/10.1002/2017JD027141>
- 1319 Pielke, R. A. (2001). Influence of the spatial distribution of vegetation and soils on the prediction
1320 of cumulus Convective rainfall. *Reviews of Geophysics*, *39*(2), 151–177.
1321 <https://doi.org/10.1029/1999RG000072>
- 1322 Polehampton, E., Cox, C., Smith, D., Ghent, D., Wooster, M., Xu, W., et al. (2022). *Copernicus*
1323 *Sentinel-3 SLSTR Land User Handbook*. Retrieved from
1324 <https://sentinel.esa.int/documents/247904/4598082/Sentinel-3-SLSTR-Land-Handbook.pdf/>
- 1325 Poltoradnev, M., Ingwersen, J., & Streck, T. (2016). Spatial and Temporal Variability of Soil
1326 Water Content in Two Regions of Southwest Germany during a Three-Year Observation
1327 Period. *Vadose Zone Journal*, *15*(6), vzj2015.11.0143.
1328 <https://doi.org/10.2136/vzj2015.11.0143>
- 1329 Van der Putten, W. H., Bardgett, R. D., Bever, J. D., Bezemer, T. M., Casper, B. B., Fukami, T.,
1330 et al. (2013). Plant-soil feedbacks: The past, the present and future challenges. *Journal of*
1331 *Ecology*, *101*(2), 265–276. <https://doi.org/10.1111/1365-2745.12054>
- 1332 Qu, W., Bogaen, H. R., Huisman, J. A., Martinez, G., Pachepsky, Y. A., & Vereecken, H.
1333 (2014). Effects of Soil Hydraulic Properties on the Spatial Variability of Soil Water
1334 Content: Evidence from Sensor Network Data and Inverse Modeling. *Vadose Zone Journal*,
1335 *13*(12), vzj2014.07.0099. <https://doi.org/10.2136/vzj2014.07.0099>
- 1336 Risser, M. D., & Turek, D. (2020). Bayesian inference for high-dimensional nonstationary
1337 Gaussian processes. *Journal of Statistical Computation and Simulation*, 2902–2928.
1338 <https://doi.org/10.1080/00949655.2020.1792472>
- 1339 Rodríguez-Iturbe, I., & Mejía, J. M. (1974). The design of rainfall networks in time and space.
1340 *Water Resources Research*, *10*(4), 713–728. <https://doi.org/10.1029/WR010i004p00713>
- 1341 Rouhani, S., & Myers, D. E. (1990). Problems in space-time kriging of geohydrological data.
1342 *Mathematical Geology*, *22*(5), 611–623. <https://doi.org/10.1007/BF00890508>
- 1343 Rudi, J., Pabel, R., Jager, G., Koch, R., Kunoth, A., & Bogaen, H. (2010). Multiscale Analysis of
1344 Hydrologic Time Series Data using the Hilbert-Huang Transform. *Vadose Zone Journal*,

- 1345 9(4), 925–942. <https://doi.org/10.2136/vzj2009.0163>
- 1346 Running, S., Mu, Q., Zhao, M., & Moreno, A. (2019). MOD16A2GF MODIS/Terra Net
1347 Evapotranspiration Gap-Filled 8-Day L4 Global 500 m SIN Grid V006 [Data set].
1348 <https://doi.org/https://doi.org/10.5067/MODIS/MOD16A2GF.006>
- 1349 Schepanski, K., Klüser, L., Heinold, B., & Tegen, I. (2015). Spatial and temporal correlation
1350 length as a measure for the stationarity of atmospheric dust aerosol distribution.
1351 *Atmospheric Environment*, 122, 10–21. <https://doi.org/10.1016/j.atmosenv.2015.09.034>
- 1352 Senatore, A., Mendicino, G., Gochis, D. J., Yu, W., Yates, D. N., & Kunstmann, H. (2015). Fully
1353 coupled atmosphere-hydrology simulations for the central Mediterranean: Impact of
1354 enhanced hydrological parameterization for short and long time scales. *Journal of Advances
1355 in Modeling Earth Systems*, 7(4), 1693–1715. <https://doi.org/10.1002/2015MS000510>
- 1356 Seyfried, M., Link, T., Marks, D., & Murdock, M. (2016). Soil Temperature Variability in
1357 Complex Terrain Measured Using Fiber-Optic Distributed Temperature Sensing. *Vadose
1358 Zone Journal*, 15(6), vzj2015.09.0128. <https://doi.org/10.2136/vzj2015.09.0128>
- 1359 Shi, L., & Bates, J. J. (2011). Three decades of intersatellite-calibrated High-Resolution Infrared
1360 Radiation Sounder upper tropospheric water vapor. *Journal of Geophysical Research:
1361 Atmospheres*, 116(D4), 4108. <https://doi.org/10.1029/2010JD014847>
- 1362 Shrestha, P., Sulis, M., Masbou, M., Kollet, S., & Simmer, C. (2014). A Scale-Consistent
1363 Terrestrial Systems Modeling Platform Based on COSMO, CLM, and ParFlow. *Monthly
1364 Weather Review*, 142(9), 3466–3483. <https://doi.org/10.1175/MWR-D-14-00029.1>
- 1365 Simon, J. S., Bragg, A. D., Dirmeyer, P. A., & Chaney, N. W. (2021). Semi-Coupling of a Field-
1366 Scale Resolving Land-Surface Model and WRF-LES to Investigate the Influence of Land-
1367 Surface Heterogeneity on Cloud Development. *Journal of Advances in Modeling Earth
1368 Systems*, 13(10), e2021MS002602. <https://doi.org/10.1029/2021MS002602>
- 1369 Sims, D. A., Rahman, A. F., Cordova, V. D., El-Masri, B. Z., Baldocchi, D. D., Bolstad, P. V., et
1370 al. (2008). A new model of gross primary productivity for North American ecosystems
1371 based solely on the enhanced vegetation index and land surface temperature from MODIS.
1372 *Remote Sensing of Environment*, 112(4), 1633–1646.
1373 <https://doi.org/10.1016/J.RSE.2007.08.004>
- 1374 Sobrino, J. A., Li, Z. L., & Stoll, M. P. (1993). Impact of the Atmospheric Transmittance and
1375 Total Water Vapor Content in the Algorithms for Estimating Satellite Sea Surface
1376 Temperatures. *IEEE Transactions on Geoscience and Remote Sensing*, 31(5), 946–952.
1377 <https://doi.org/10.1109/36.263765>
- 1378 Stein, M. L. (1999). *Interpolation of Spatial Data : Some Theory for Kriging*. New York, NY:
1379 Springer.
- 1380 Stein, M. L. (2005). Space-time covariance functions. *Journal of the American Statistical
1381 Association*, 100(469), 310–321. <https://doi.org/10.1198/016214504000000854>
- 1382 Stisen, S., McCabe, M. F., Refsgaard, J. C., Lerer, S., & Butts, M. B. (2011). Model parameter
1383 analysis using remotely sensed pattern information in a multi-constraint framework. *Journal
1384 of Hydrology*, 409(1–2), 337–349. <https://doi.org/10.1016/j.jhydrol.2011.08.030>
- 1385 Stisen, S., Soltani, M., Mendiguren, G., Langkilde, H., Garcia, M., & Koch, J. (2021). Spatial

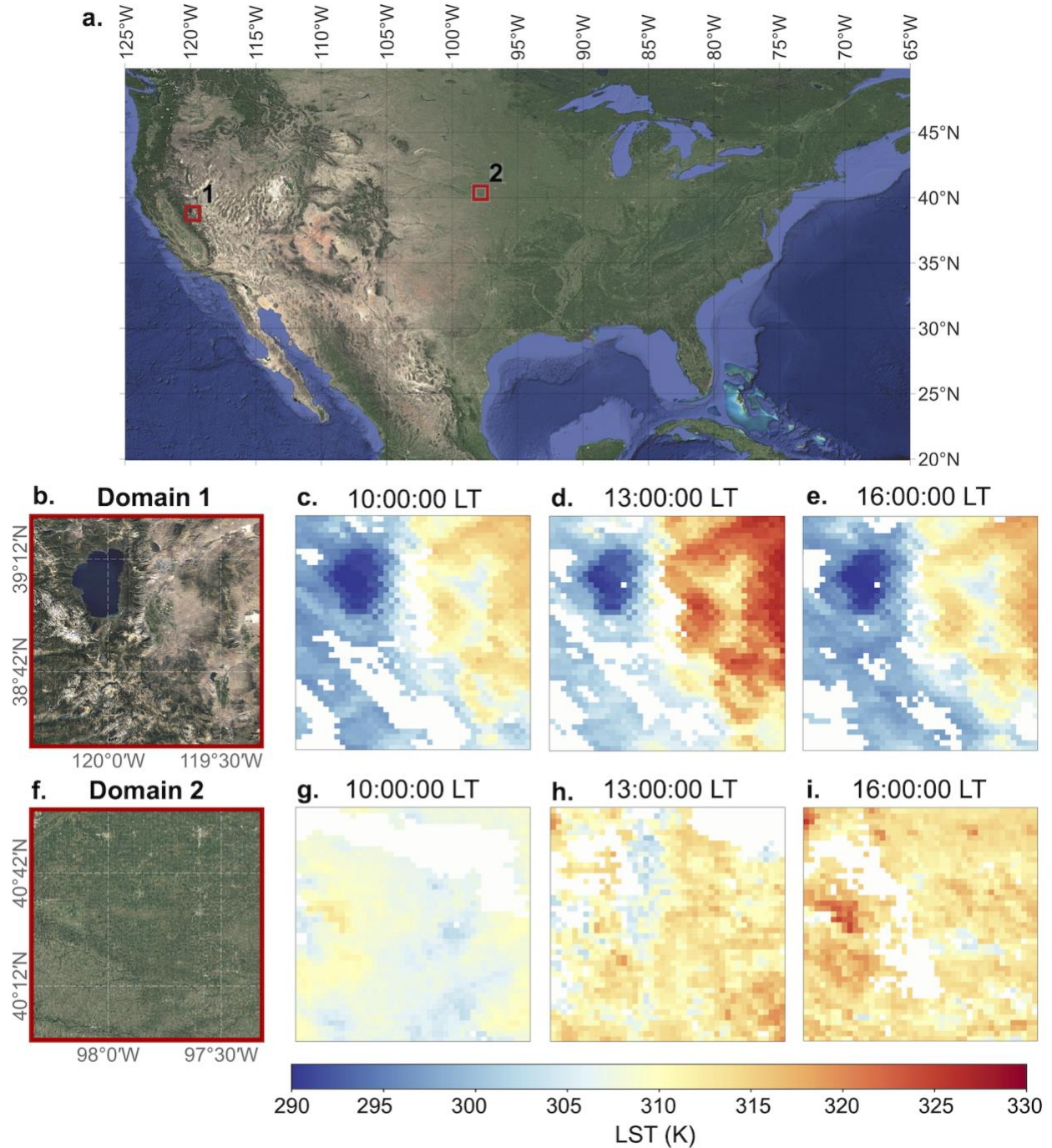
- 1386 patterns in actual evapotranspiration climatologies for europe. *Remote Sensing*, 13(12).
1387 <https://doi.org/10.3390/rs13122410>
- 1388 Stoy, P. C., Katul, G., Siqueira, M. B. S., Juang, J. Y., McCarthy, H. R., Kim, H. S., et al. (2005).
1389 Variability in net ecosystem exchange from hourly to inter-annual time scales at adjacent
1390 pine and hardwood forests: A wavelet analysis. *Tree Physiology*, 25(7), 887–902.
1391 <https://doi.org/10.1093/treephys/25.7.887>
- 1392 Su, Z. (2002). The Surface Energy Balance System (SEBS) for estimation of turbulent heat
1393 fluxes. *Hydrology and Earth System Sciences*, 6(1), 85–99. [https://doi.org/10.5194/hess-6-](https://doi.org/10.5194/hess-6-85-2002)
1394 [85-2002](https://doi.org/10.5194/hess-6-85-2002)
- 1395 Sušelj, K., Teixeira, J., & Chung, D. (2013). A Unified Model for Moist Convective Boundary
1396 Layers Based on a Stochastic Eddy-Diffusivity/Mass-Flux Parameterization. *Journal of the*
1397 *Atmospheric Sciences*, 70(7), 1929–1953. <https://doi.org/10.1175/JAS-D-12-0106.1>
- 1398 Talbot, C., Bou-Zeid, E., & Smith, J. (2012). Nested Mesoscale Large-Eddy Simulations with
1399 WRF: Performance in Real Test Cases. *Journal of Hydrometeorology*, 13(5), 1421–1441.
1400 <https://doi.org/10.1175/JHM-D-11-048.1>
- 1401 Tapley, B. D., Bettadpur, S., Ries, J. C., Thompson, P. F., & Watkins, M. M. (2004). GRACE
1402 measurements of mass variability in the Earth system. *Science*, 305(5683), 503–505.
1403 https://doi.org/10.1126/SCIENCE.1099192/SUPPL_FILE/TAPLEY.SOM.PDF
- 1404 Taylor, C. M., Parker, D. J., & Harris, P. P. (2007). An observational case study of mesoscale
1405 atmospheric circulations induced by soil moisture. *Geophysical Research Letters*, 34(15).
1406 <https://doi.org/10.1029/2007GL030572>
- 1407 Taylor, C. M., Parker, D. J., Kalthoff, N., Gaertner, M. A., Philippon, N., Bastin, S., et al. (2011).
1408 New perspectives on land-atmosphere feedbacks from the African Monsoon
1409 Multidisciplinary Analysis. *Atmospheric Science Letters*, 12(1), 38–44.
1410 <https://doi.org/10.1002/asl.336>
- 1411 Taylor, C. M., Birch, C. E., Parker, D. J., Dixon, N., Guichard, F., Nikulin, G., & Lister, G. M. S.
1412 (2013). Modeling soil moisture-precipitation feedback in the Sahel: Importance of spatial
1413 scale versus convective parameterization. *Geophysical Research Letters*, 40(23), 6213–
1414 6218. <https://doi.org/10.1002/2013GL058511>
- 1415 Tesfa, T. K., Li, H.-Y., Leung, L. R., Huang, M., Ke, Y., Sun, Y., & Liu, Y. (2014). A subbasin-
1416 based framework to represent land surface processes in an Earth system model. *Geosci.*
1417 *Model Dev*, 7, 947–963. <https://doi.org/10.5194/gmd-7-947-2014>
- 1418 Timmermans, W. J., Bertoldi, G., Albertson, J. D., Olioso, A., Su, Z., & Gieske, A. S. M. (2010).
1419 Accounting for atmospheric boundary layer variability on flux estimation from RS
1420 observations. <https://doi.org/10.1080/01431160802036383>, 29(17–
1421 18), 5275–5290. <https://doi.org/10.1080/01431160802036383>
- 1422 Tobler, W. R. (1970). A Computer Movie Simulating Urban Growth in the Detroit Region.
1423 *Economic Geography*, 46, 234. <https://doi.org/10.2307/143141>
- 1424 Torres-Rojas, L., & Chaney, N. W. (2023). Supporting Dataset: The observed spatio-temporal
1425 patterns of Land surface temperature over the Contiguous United States.
1426 <https://doi.org/10.5281/ZENODO.8428629>

- 1427 Torres-Rojas, L., Vergopolan, N., Herman, J. D., & Chaney, N. W. (2022). Towards an Optimal
1428 Representation of Sub-Grid Heterogeneity in Land Surface Models. *Water Resources*
1429 *Research*, 58(12), e2022WR032233. <https://doi.org/10.1029/2022WR032233>
- 1430 Tsai, Y.-L. S., Dietz, A., Oppelt, N., Kuenzer, C., De (A. D., Kuenzer@dlr, C., & De, C. K.
1431 (2019). Remote Sensing of Snow Cover Using Spaceborne SAR: A Review. *Remote*
1432 *Sensing 2019, Vol. 11, Page 1456, 11(12)*, 1456. <https://doi.org/10.3390/RS11121456>
- 1433 Tuttle, S., & Salvucci, G. (2016). Empirical evidence of contrasting soil moisture–precipitation
1434 feedbacks across the United States. *Science*, 352(6287), 825–828.
1435 <https://doi.org/10.1126/science.aaa7185>
- 1436 Vargas, R., Detto, M., Baldocchi, D. D., & Allen, M. F. (2010). Multiscale analysis of temporal
1437 variability of soil CO₂ production as influenced by weather and vegetation. *Global Change*
1438 *Biology*, 16(5), 1589–1605. <https://doi.org/10.1111/j.1365-2486.2009.02111.x>
- 1439 Varouchakis, E. A. (2018). *Background of spatiotemporal geostatistical analysis: Application to*
1440 *aquifer level mapping. Spatiotemporal Analysis of Extreme Hydrological Events*. Elsevier
1441 Inc. <https://doi.org/10.1016/B978-0-12-811689-0.00002-1>
- 1442 Vereecken, H., Huisman, J. A., Bogaen, H., Vanderborght, J., Vrugt, J. A., & Hopmans, J. W.
1443 (2008). On the value of soil moisture measurements in vadose zone hydrology: A review.
1444 *Water Resources Research*, 46(4). <https://doi.org/10.1029/2008WR006829>
- 1445 Vereecken, H., Pachepsky, Y., Simmer, C., Rihani, J., Kunoth, A., Korres, W., et al. (2016). On
1446 the role of patterns in understanding the functioning of soil-vegetation-atmosphere systems.
1447 *Journal of Hydrology*, 542, 63–86. <https://doi.org/10.1016/j.jhydrol.2016.08.053>
- 1448 Vergopolan, N., Chaney, N. W., Pan, M., Sheffield, J., Beck, H. E., Ferguson, C. R., et al.
1449 (2021). SMAP-HydroBlocks, a 30-m satellite-based soil moisture dataset for the
1450 conterminous US. *Scientific Data 2021 8:1*, 8(1), 1–11. [https://doi.org/10.1038/s41597-021-](https://doi.org/10.1038/s41597-021-01050-2)
1451 [01050-2](https://doi.org/10.1038/s41597-021-01050-2)
- 1452 Vergopolan, N., Sheffield, J., Chaney, N. W., Pan, M., Beck, H. E., Ferguson, C. R., et al.
1453 (2022). High-Resolution Soil Moisture Data Reveal Complex Multi-Scale Spatial
1454 Variability Across the United States. *Geophysical Research Letters*, 49(15),
1455 e2022GL098586. <https://doi.org/10.1029/2022GL098586>
- 1456 Wagner, D., Ruprecht, E., & Simmer, C. (1990). A Combination of Microwave Observations
1457 from Satellites and an EOF Analysis to Retrieve Vertical Humidity Profiles over the Ocean.
1458 *Journal of Applied Meteorology*, 29(11), 1142–1157. [https://doi.org/10.1175/1520-](https://doi.org/10.1175/1520-0450(1990)029<1142:ACOMOF>2.0.CO;2)
1459 [0450\(1990\)029<1142:ACOMOF>2.0.CO;2](https://doi.org/10.1175/1520-0450(1990)029<1142:ACOMOF>2.0.CO;2)
- 1460 Wagner, W., Hahn, S., Kidd, R., Melzer, T., Bartalis, Z., Hasenauer, S., et al. (2013). The
1461 ASCAT Soil Moisture Product: A Review of its Specifications, Validation Results, and
1462 Emerging Applications. *Meteorologische Zeitschrift*, 22(1), 5–33.
1463 <https://doi.org/10.1127/0941-2948/2013/0399>
- 1464 Wainwright, H. M., Uhlemann, S., Franklin, M., Falco, N., Bouskill, N. J., Newcomer, M. E., et
1465 al. (2022). Watershed zonation through hillslope clustering for tractably quantifying above-
1466 and below-ground watershed heterogeneity and functions. *Hydrology and Earth System*
1467 *Sciences*, 26(2), 429–444. <https://doi.org/10.5194/hess-26-429-2022>

- 1468 Wan, Z. (1996). A generalized split-window algorithm for retrieving land-surface temperature
1469 from space. *IEEE Transactions on Geoscience and Remote Sensing*, 34(4), 892–905.
1470 <https://doi.org/10.1109/36.508406>
- 1471 Wan, Z. (2014). New refinements and validation of the collection-6 MODIS land-surface
1472 temperature/emissivity product. *Remote Sensing of Environment*, 140, 36–45.
1473 <https://doi.org/10.1016/J.RSE.2013.08.027>
- 1474 Wang, K., & Dickinson, R. E. (2012). A review of global terrestrial evapotranspiration:
1475 Observation, modeling, climatology, and climatic variability. *Reviews of Geophysics*, 50(2),
1476 2005. <https://doi.org/10.1029/2011RG000373>
- 1477 Wang, Y., Liu, H., Liu, Y., Wang, S., Wang, L., & Li, X. (2023). Effect of land–atmosphere
1478 process parameterizations on the PM simulation of a river valley city with complex
1479 topography. *Atmospheric Research*, 281(October 2022), 106505.
1480 <https://doi.org/10.1016/j.atmosres.2022.106505>
- 1481 Wealands, S. R., Grayson, R. B., & Walker, J. P. (2005). Quantitative comparison of spatial
1482 fields for hydrological model assessment - Some promising approaches. *Advances in Water*
1483 *Resources*, 28(1), 15–32. <https://doi.org/10.1016/j.advwatres.2004.10.001>
- 1484 Weaver, C. P. (2004). Coupling between large-scale atmospheric processes and mesoscale land-
1485 atmosphere interactions in the U.S. Southern Great Plains during summer. Part I: Case
1486 studies. *Journal of Hydrometeorology*, 5(6), 1223–1246. <https://doi.org/10.1175/JHM-396.1>
- 1487 Wu, C., Lo, M., Chen, W., & Lu, C. (2015). The impacts of heterogeneous land surface fluxes on
1488 the diurnal cycle precipitation: A framework for improving the GCM representation of land-
1489 atmosphere interactions. *Journal of Geophysical Research: Atmospheres*, 120(9), 3714–
1490 3727. <https://doi.org/10.1002/2014JD023030>
- 1491 Xiao, M., Mascaro, G., Wang, Z., Whitney, K. M., & Vivoni, E. R. (2022). On the value of
1492 satellite remote sensing to reduce uncertainties of regional simulations of the Colorado
1493 River. *Hydrology and Earth System Sciences*, 26(21), 5627–5646.
1494 <https://doi.org/10.5194/hess-26-5627-2022>
- 1495 Xu, F., & Ignatov, A. (2014). In situ SST quality monitor (iQuam). *Journal of Atmospheric and*
1496 *Oceanic Technology*, 31(1), 164–180. <https://doi.org/10.1175/JTECH-D-13-00121.1>
- 1497 Yu, Y., & Yu, P. (2020). Land Surface Temperature Product from the GOES-R Series. In *The*
1498 *GOES-R Series* (pp. 133–144). Elsevier. [https://doi.org/10.1016/B978-0-12-814327-](https://doi.org/10.1016/B978-0-12-814327-8.00012-3)
1499 [8.00012-3](https://doi.org/10.1016/B978-0-12-814327-8.00012-3)
- 1500 Yu, Y., Tarpley, D., Hui, X., & Chen, M. (2012). *GOES-R Advanced Baseline Imager (ABI)*
1501 *Algorithm Theoretical Basis Document For Land Surface Temperature* (Version 2.). NOAA
1502 NESDIS, Center for Satellite Applications and Research.
- 1503 Zink, M., Mai, J., Cuntz, M., & Samaniego, L. (2018). Conditioning a Hydrologic Model Using
1504 Patterns of Remotely Sensed Land Surface Temperature. *Water Resources Research*, 54(4),
1505 2976–2998. <https://doi.org/10.1002/2017WR021346>

1506

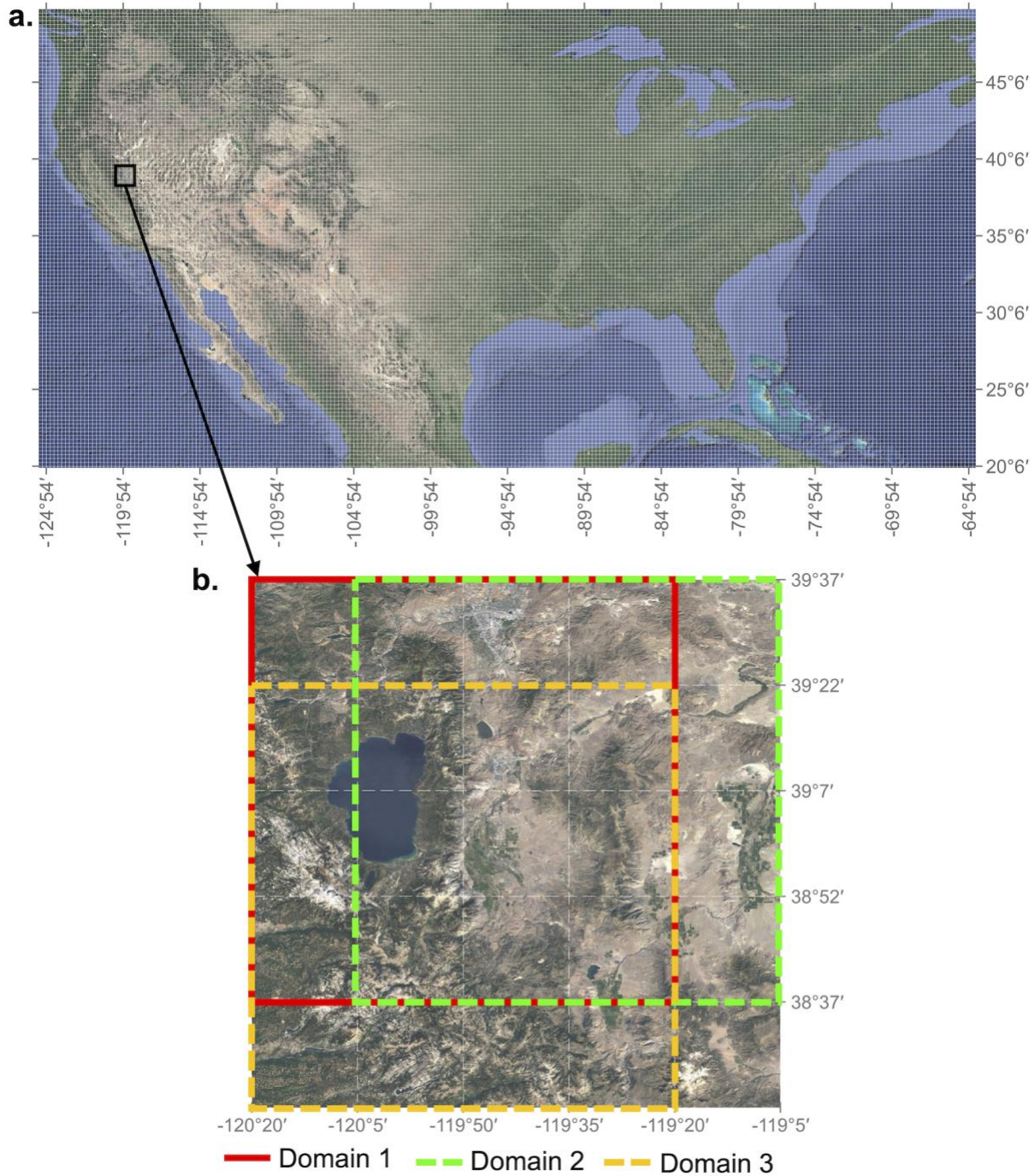
1507



1508

1509 **Figure 1.** Temporal evolution of LST over two $1.0^{\circ} \times 1.0^{\circ}$ domains over CONUS on 2020-07-04.
 1510 a) Location of the domains within CONUS; b and f) zoomed-in satellite visible imagery with
 1511 coordinates, c and g) GOES-16 derived LST for 10:00:00 local time (LT); d and h) 13:00:00 LT,
 1512 and e and i) 16:00:00 LT.

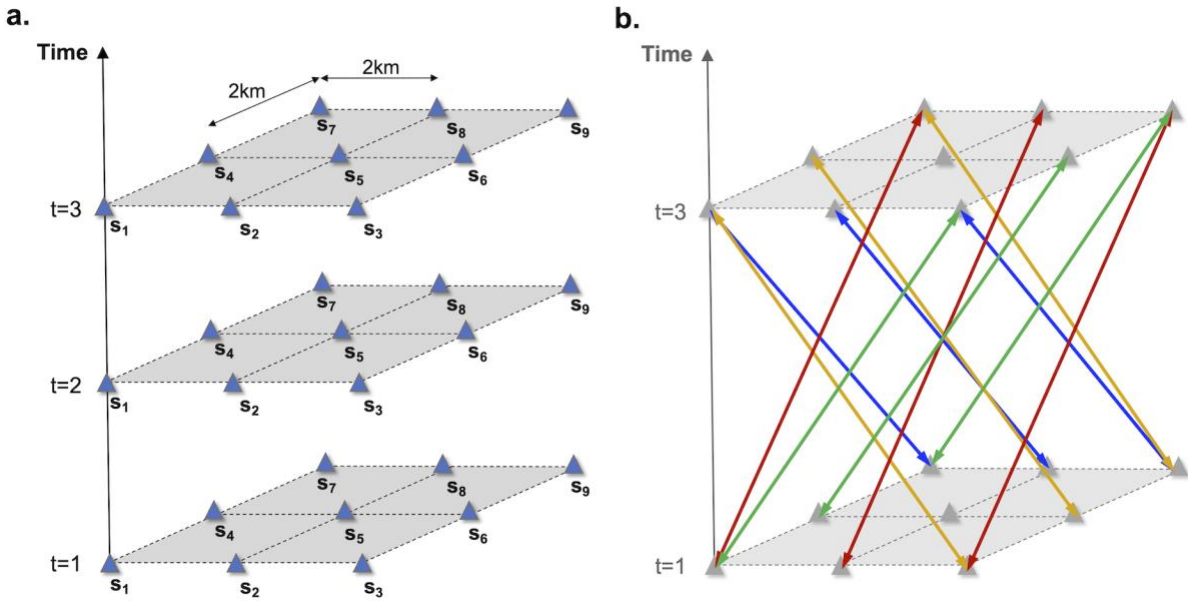
1513



1514

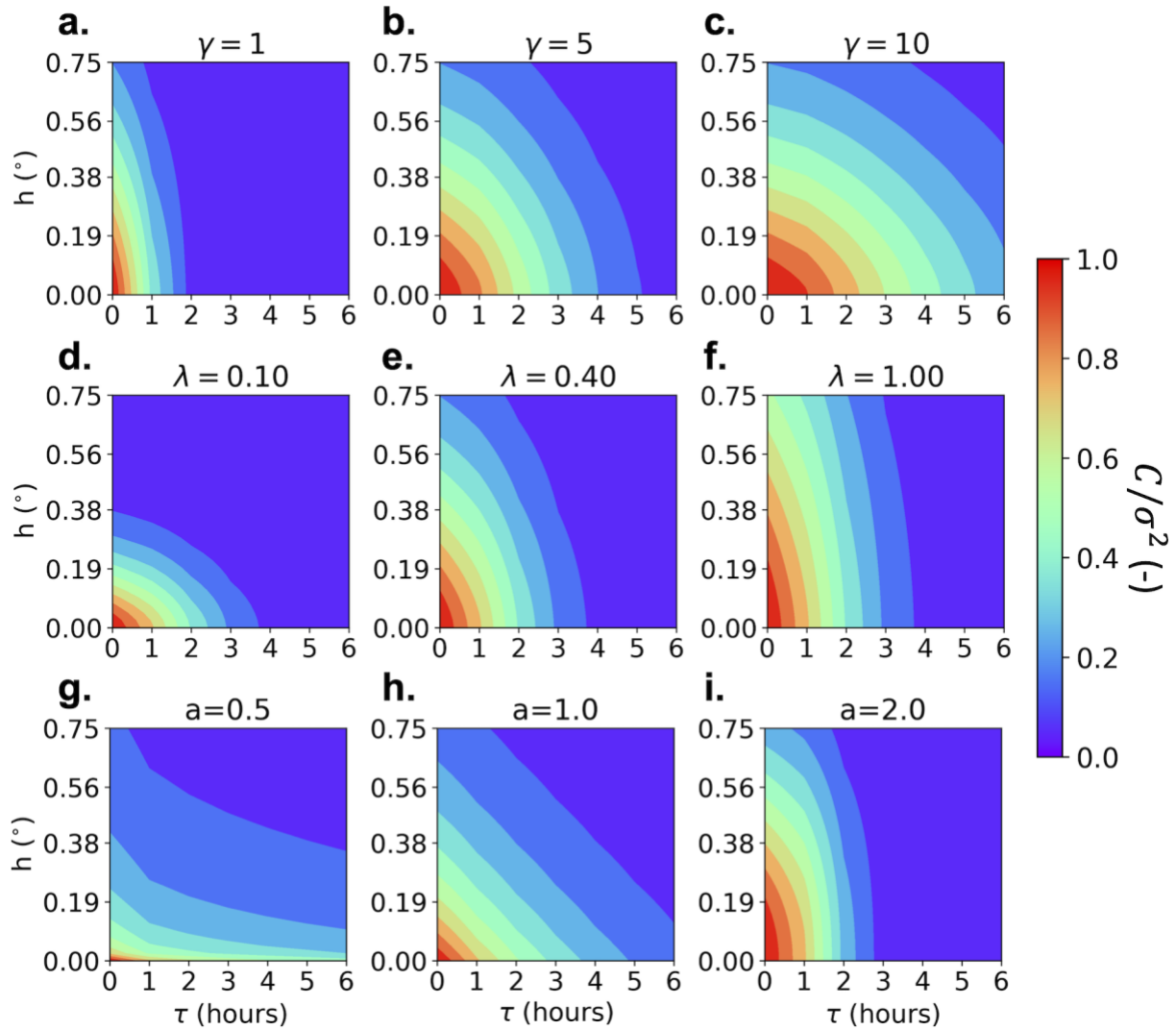
1515 **Figure 2.** Study domain over CONUS and detail of the sliding window approach used. a) Study
 1516 domain over CONUS; the central 0.25° of each 1.0°x1.0° squared box obtained from the sliding
 1517 window approach is presented as the grid; coordinates every 5° are presented to aid in
 1518 georeferencing. b) Detail of the sliding window approach used for sampling over a domain in the
 1519 California-Nevada border. Three (3) 1.0°x1.0° domains separated by 0.25° from domain 1 in the
 1520 horizontal (domain 2) and vertical (domain 3) directions are displayed.

1521



1522

1523 **Figure 3.** a) Schematic view of a regularly-spaced 2-kilometer grid over a time axis with 3
 1524 compartments; b) 12 pairs of points separated by a spatial distance of 4km and a temporal lag of
 1525 2 ($(h, u) = (4km, 2)$), colors represent sides of the spatial grid where the origin point is located:
 1526 yellow for left, red for back, green for right, and blue for front.
 1527



1528

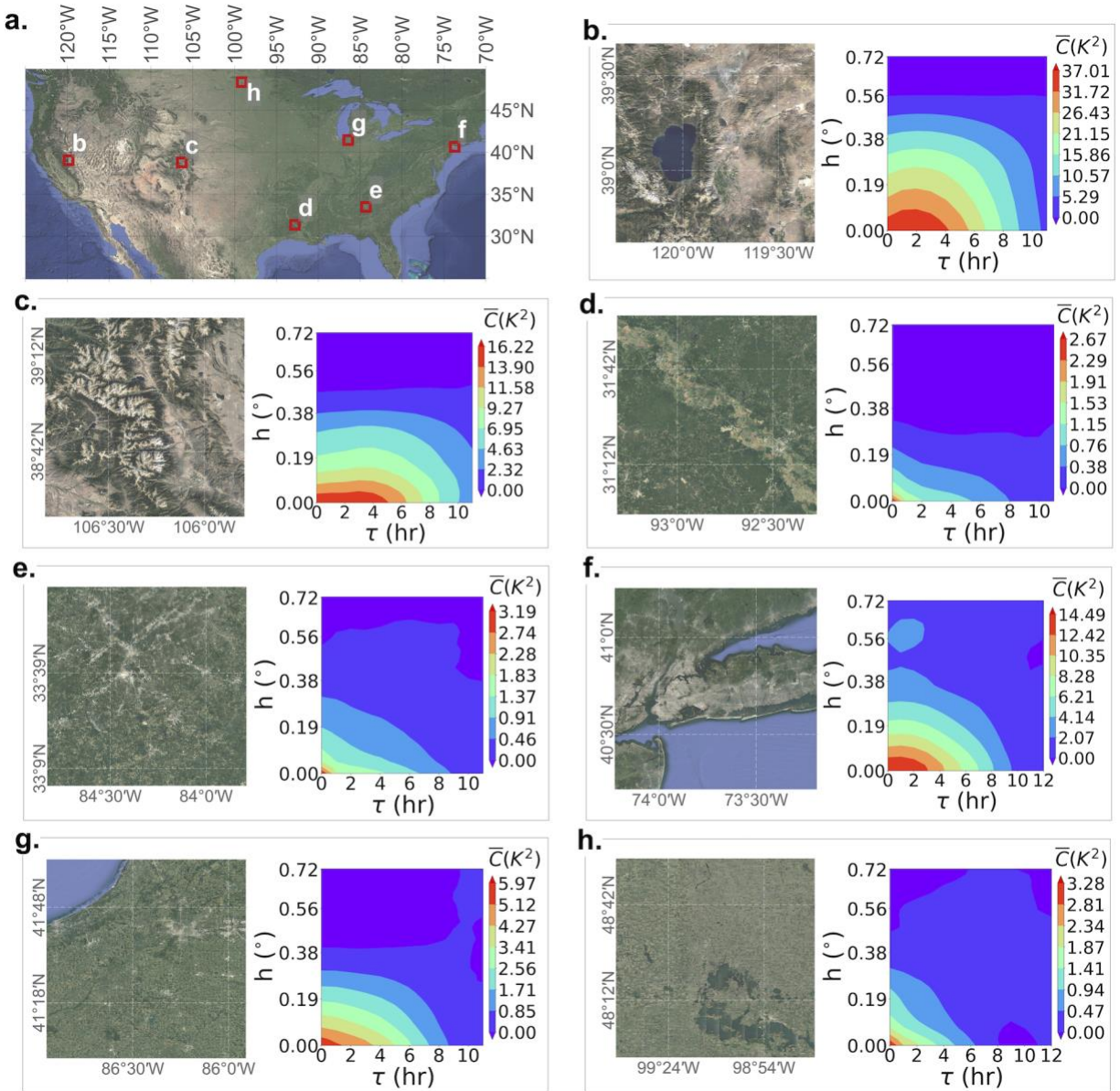
1529

1530

1531

1532

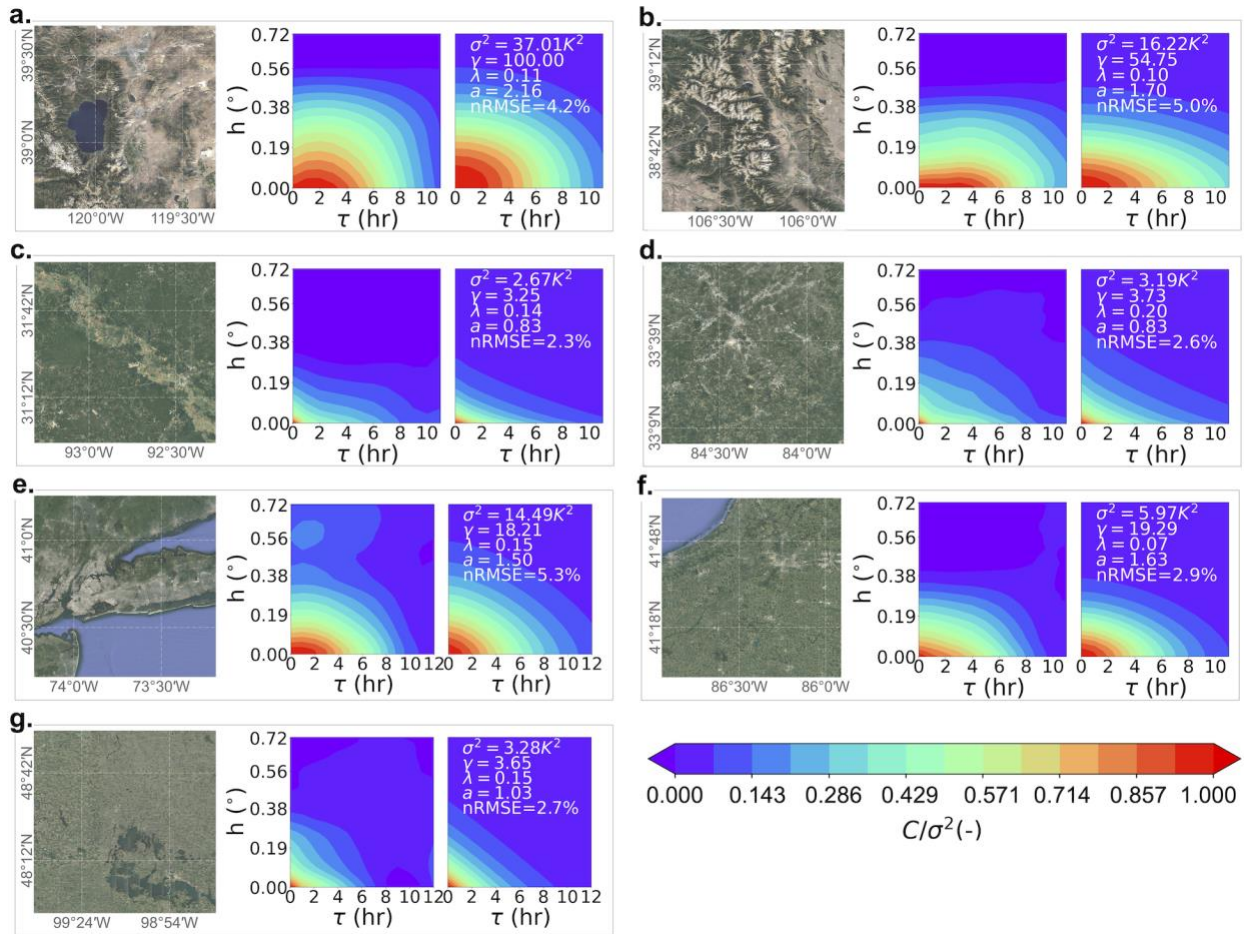
Figure 4. Parametric spatio-temporal covariance function obtained by individually increasing the values of the three main model parameters: a, b, and c) varying γ with $\lambda = 0.4$ and $a = 1.5$; d, e, and f) varying λ with $\gamma = 3$ and $a = 1.5$; and g, h, and i) varying a with $\lambda = 0.4$ and $\gamma = 3$.



1533

1534 **Figure 5.** Zoomed-in satellite visible imagery with coordinates for seven $1.0^\circ \times 1.0^\circ$ domains over
 1535 CONUS. The obtained summer daytime LST ESTCFs for each domain are also presented. a)
 1536 Location of the seven domains within CONUS; visible satellite imagery of the landscape and
 1537 computed ESTCF for b) the Lake Tahoe area, California-Nevada border; c) the Mount Mitchell
 1538 area, Colorado; d) Mississippi River, Louisiana; e) Atlanta, Georgia; f) New York City; g) Lake
 1539 Michigan shore, Indiana-Michigan border; h) Leeds county, North Dakota.

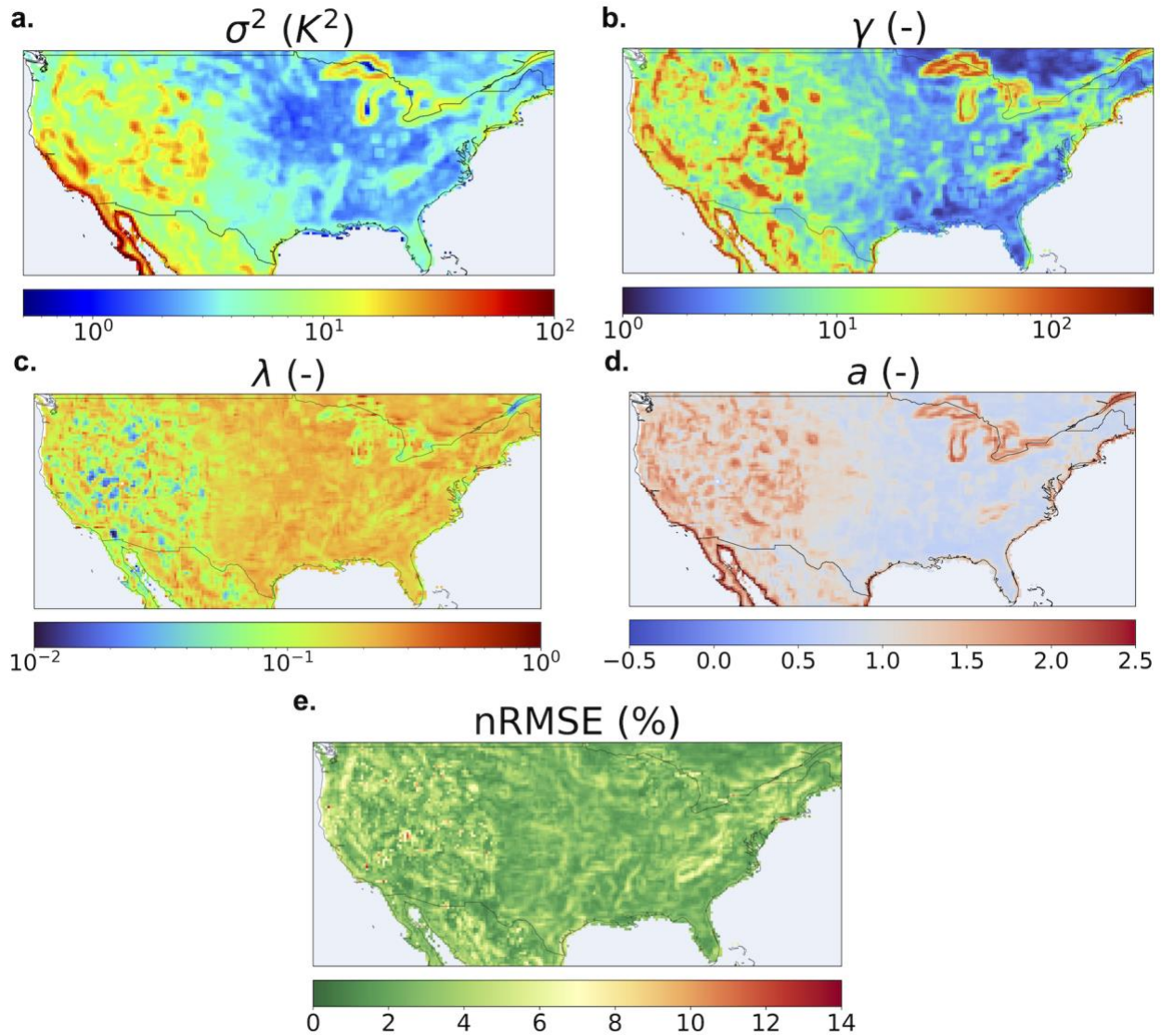
1540



1541

1542 **Figure 6.** Zoomed-in satellite visible imagery with coordinates for the seven $1.0^\circ \times 1.0^\circ$ domains
 1543 over CONUS. The obtained summer daytime LST ESTCFs for each domain and the fitted
 1544 spatio-temporal covariance function parametric model are presented. The plots for the fitted
 1545 cases include the obtained set of parameters and the normalized root mean square error (nRMSE)
 1546 for the fit. Visible satellite imagery of the landscape, computed ESTCF, and fitted spatio-
 1547 temporal covariance function parametric model for a) the Lake Tahoe area, California-Nevada
 1548 border; b) the Mount Mitchell area, Colorado; c) Mississippi River, Louisiana; d) Atlanta,
 1549 Georgia; e) New York City; f) Lake Michigan shore, Indiana-Michigan border; g) Leeds county,
 1550 North Dakota.

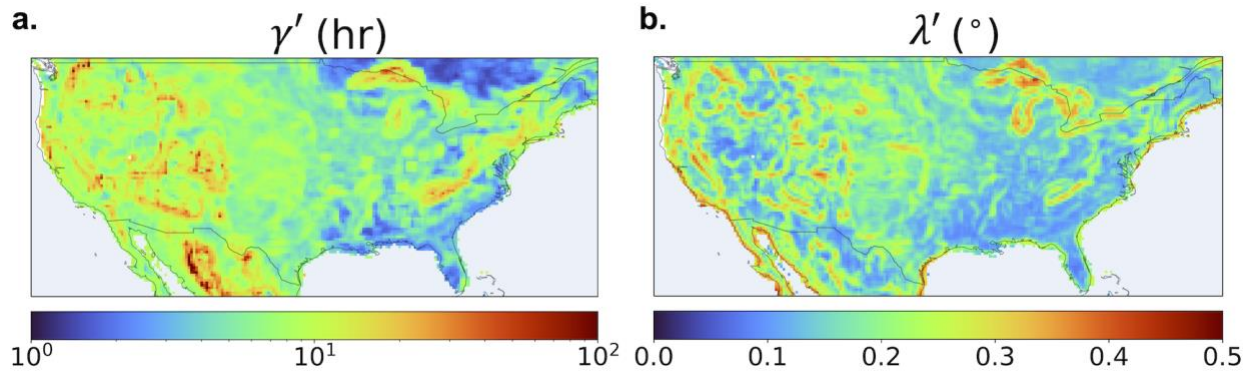
1551



1552

1553 **Figure 7.** Maps of results for the parametric spatio-temporal covariance function fit for land-
 1554 containing domains. Each pixel represents the central $0.25^\circ \times 0.25^\circ$ for each $1.0^\circ \times 1.0^\circ$ analyzed
 1555 domain. a) Computed spatio-temporal variance, b) fitted temporal characteristic length-scale, c)
 1556 fitted spatial characteristic length-scale, d) fitted spatio-temporal interaction exponent, and e)
 1557 nRMSE for the parametric fit.

1558



1559

1560

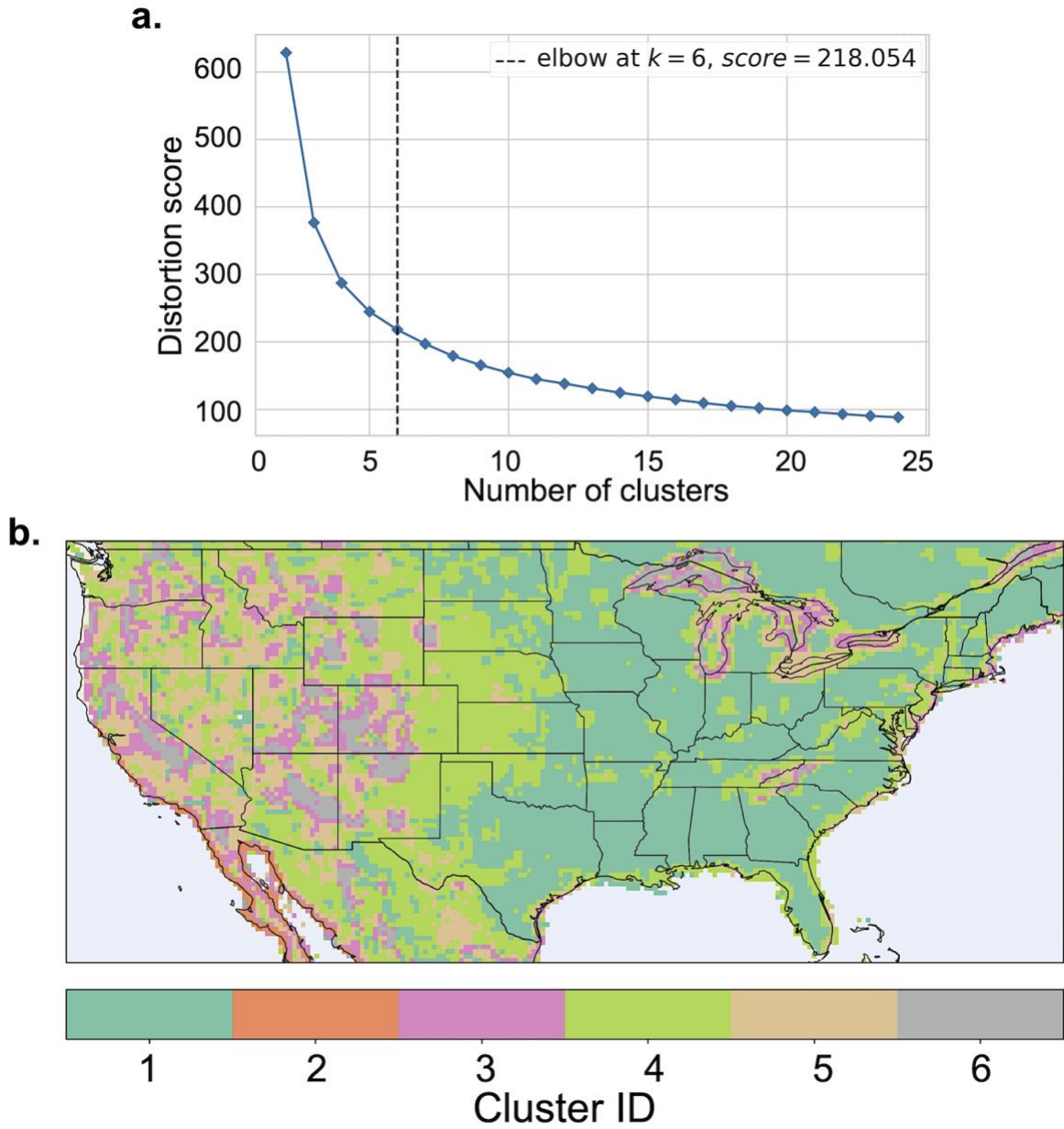
1561

1562

1563

1564

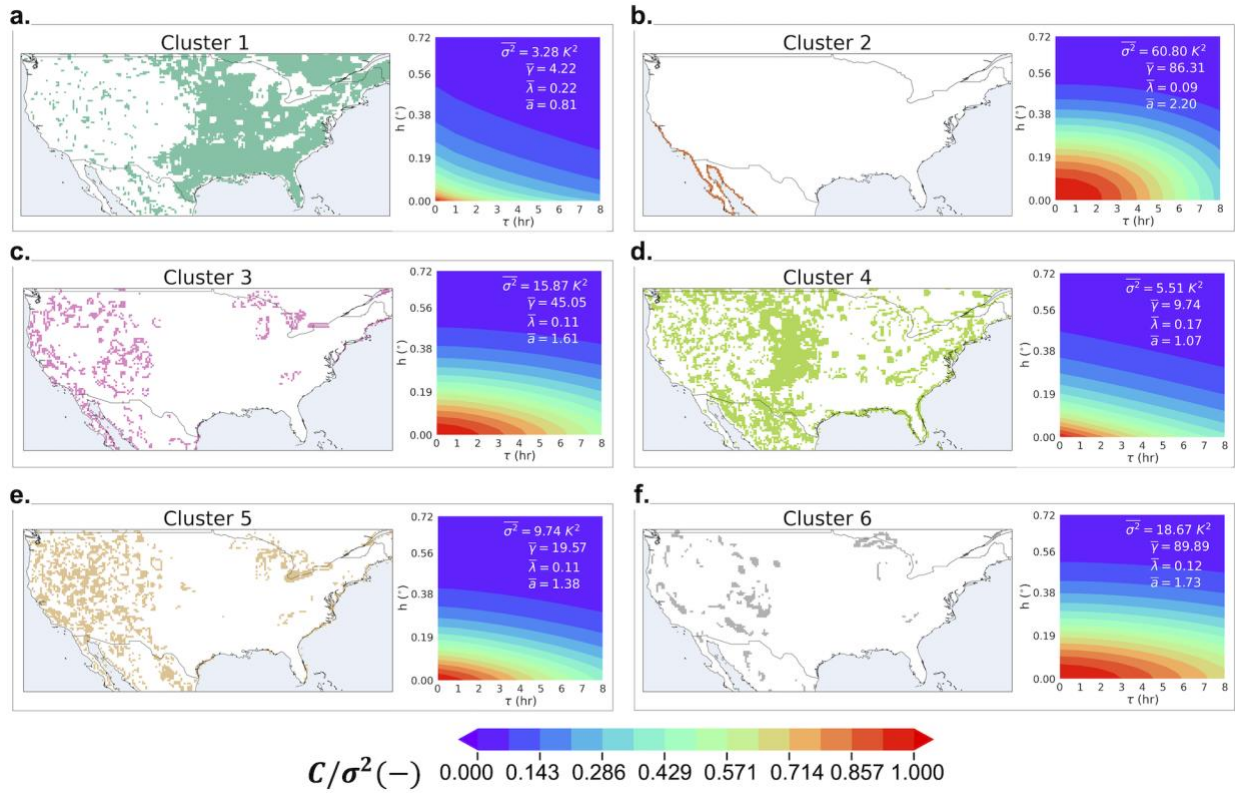
Figure 8. Maps of results for the modified forms of the spatio-temporal characteristic length scales for land-containing domains. Each pixel represents the central $0.25^\circ \times 0.25^\circ$ for each $1.0^\circ \times 1.0^\circ$ analyzed domain. a) Modified temporal characteristic length-scale, b) modified spatial characteristic length-scale.



1565

1566 **Figure 9.** a) Elbow diagram for cluster number determination and, b) spatial maps of obtained
1567 clusters over CONUS.

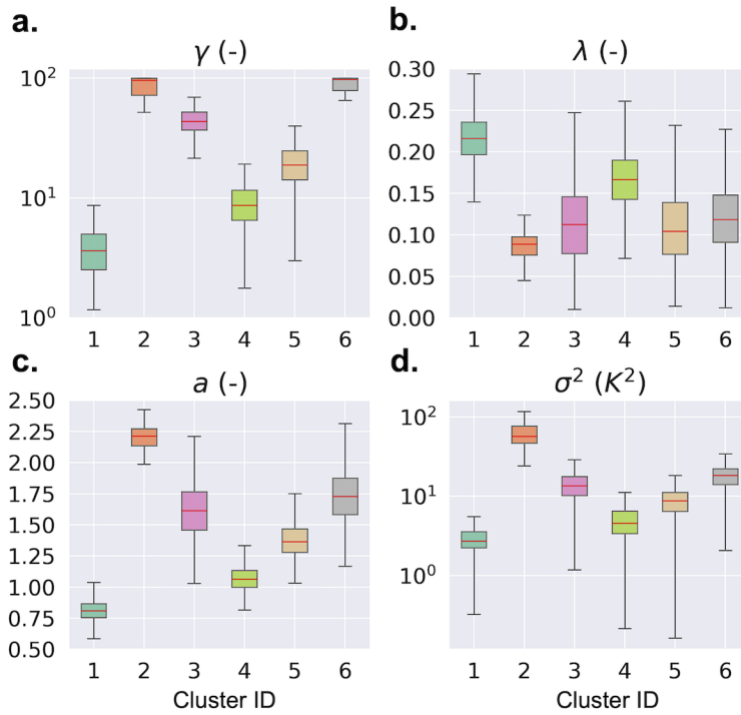
1568



1569

1570 **Figure 10.** Individual spatial mapping of the clusters over CONUS, next to the corresponding
 1571 characteristic spatio-temporal covariance function (CSTCF) obtained as the mean cluster value of
 1572 the parameters for a) cluster 1, b) cluster 2, c) cluster 3, d) cluster 4, e) cluster 5, and f) cluster 6.

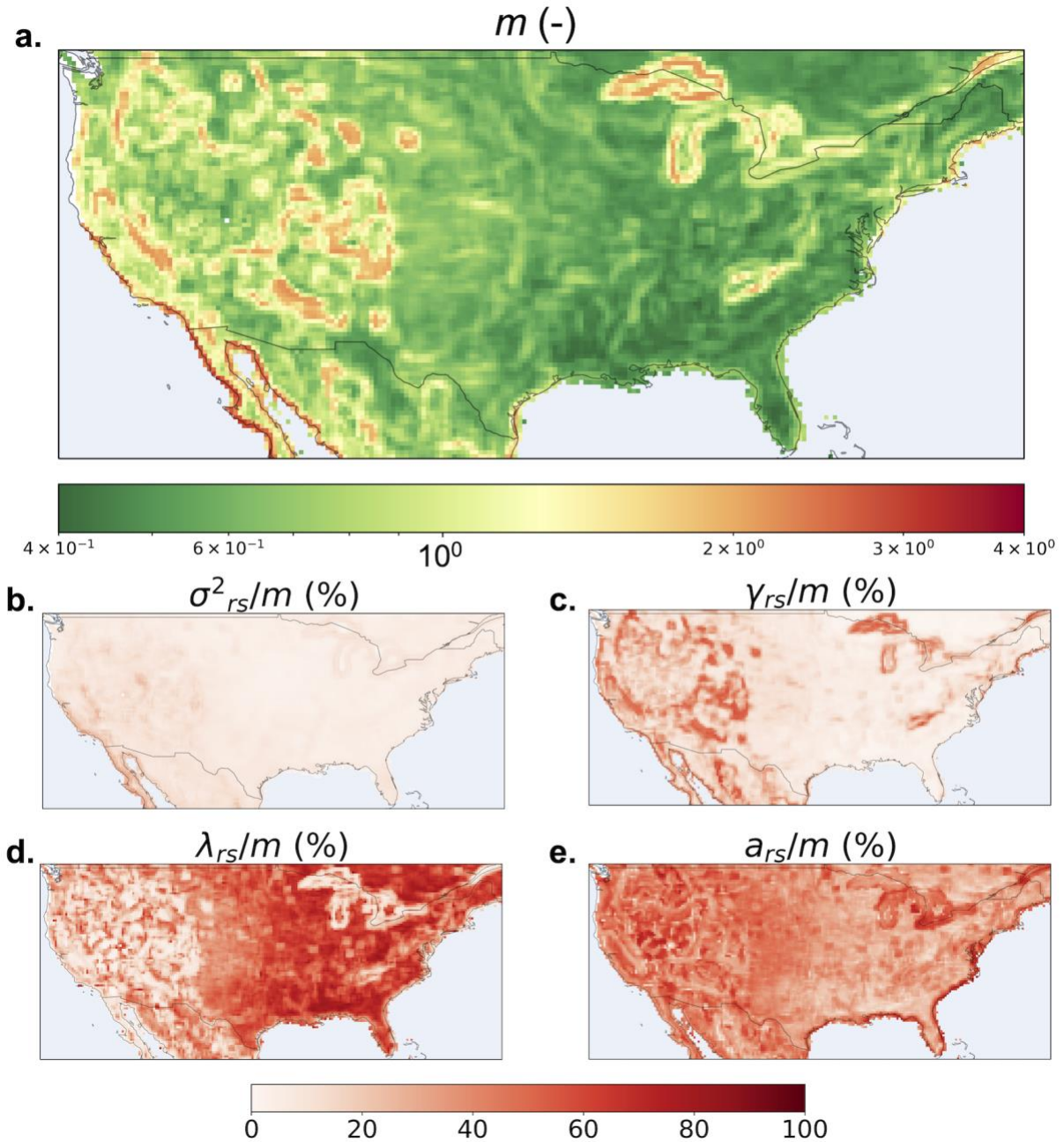
1573



1574

1575 **Figure 11.** Box plots of parameters distributions among clusters: a) characteristic temporal length-
 1576 scale, b) characteristic spatial length-scale, c) spatio-temporal interaction exponent, and d) spatio-
 1577 temporal variance.

1578



1579

1580 **Figure 12.** a) Combined metric for spatio-temporal persistence for every domain in CONUS along
 1581 with individual contributions of rescaled forms of model parameters to the total metric value: b)
 1582 spatio-temporal variance, c) temporal characteristic length-scale, d) spatial characteristic length-
 1583 scale, and e) spatio-temporal interaction exponent.

1584